

Tuning the Spin Interaction in Non-planar Organic Diradicals Through Mechanical Manipulation

Alessio Vegliante,¹ Saleta Fernandez,² Ricardo Ortiz,³ Manuel Vilas-Varela,² Thomas Baum,⁴ Niklas Friedrich,¹ Francisco Romero Lara,¹ Andrea Aguirre,⁵ Katerina Vaxevani,¹ Dongfei Wang,¹ Carlos García,³ Herre S. J. van der Zant,⁴ Thomas Frederiksen,^{3,6,*} Diego Peña,^{2,†} and Jose Ignacio Pascual^{1,6,‡}

¹*CIC nanoGUNE-BRTA, 20018 Donostia-San Sebastián, Spain*

²*Centro Singular de Investigación en Química Biológica e Materiais Moleculares (CiQUS) and Departamento de Química Orgánica,*

Universidade de Santiago de Compostela 15782-Santiago de Compostela (Spain)

³*Donostia International Physics Center (DIPC), 20018 Donostia-San Sebastián, Spain*

⁴*Kavli Institute of Nanoscience, Delft University of Technology, 2628 Delft, The Netherlands*

⁵*Centro de Física de Materiales CSIC/UPV-EHU-Materials Physics Center, 20018 Donostia-San Sebastián, Spain*

⁶*IKERBASQUE, Basque Foundation for Science, 48013 Bilbao, Spain*

(Dated: February 14, 2024)

Open-shell polycyclic aromatic hydrocarbons (PAHs) represent promising building blocks for carbon-based functional magnetic materials. Their magnetic properties stem from the presence of unpaired electrons localized in radical states of π character. Consequently, these materials are inclined to exhibit spin delocalization, form extended collective states, and respond to the flexibility of the molecular backbones. However, they are also highly reactive, requiring structural strategies to protect the radical states from reacting with the environment. Here, we demonstrate that the open-shell ground state of the diradical **2-OS** survives on a Au(111) substrate as a global singlet formed by two unpaired electrons with anti-parallel spins coupled through a conformational dependent interaction. The **2-OS** molecule is a “protected” derivative of the Chichibabin’s diradical, featuring a non-planar geometry that destabilizes the closed-shell quinoidal structure. Using scanning tunneling microscopy (STM), we localized the two interacting spins at the molecular edges, and detected an excited triplet state a few millielectronvolts above the singlet ground state. Mean-field Hubbard simulations reveal that the exchange coupling between the two spins strongly depends on the torsional angles between the different molecular moieties, suggesting the possibility of influencing the molecule’s magnetic state through structural changes. This was demonstrated here using the STM tip to manipulate the molecular conformation, while simultaneously detecting changes in the spin excitation spectrum. Our work suggests the potential of these PAHs for a new class of all-carbon spin-crossover materials.

Carbon-based molecular nanostructures can exhibit magnetic states associated with the stabilization of unpaired electrons in radical sites [1]. Intrinsic π -magnetism has been widely observed in polycyclic aromatic hydrocarbons (PAHs) with an open-shell ground state, i.e., possessing one or more unpaired π electrons [2–5]. Compared to traditional inorganic materials, the magnetism associated with these systems features longer spin coherence times and more delocalized magnetic moments, combined with a high degree of chemical and mechanical tunability [6–8]. In this context, organic diradicals are of fundamental interest for understanding magnetic interactions at the molecular scale and developing control strategies [9]. Overall, open-shell organic systems have the potential to become a new class of functional magnetic materials with applications in diverse technologies such as sensorics, non-linear optics, or spintronics [10–15].

A classical example of open-shell PAH is the Chichibabin’s hydrocarbon, a molecule that has been ex-

tensively investigated for its large diradical character in the ground state [16, 17]. To circumvent its high reactivity, several derivatives have been prepared, one of the latest examples being a stable compound reported by Zeng et al. (**2-OS**, Figure 1a) [18]. The **2-OS** molecule consists of a central bisanthracene unit linked to two fluorenyl termini that accumulate the radical character of the system. The steric hindrance between fluorenyl and anthracene moieties determines a highly non-planar structure that is responsible for the protection of the radical centers, which remain localized over the fluorenyl subunits. Owing to high stability of its diradical ground state and its tuneable non-planar structure, **2-OS** is a suitable system to explore the relationship between magnetism and geometry at the single molecule scale.

A triplet ground state was reported for **2-OS** in solution, in agreement with DFT calculations of the magnetic state of the molecule in the gas phase [18]. Recently, **2-OS** was also studied in mechanically controlled break-junction devices [19], where spectroscopic features

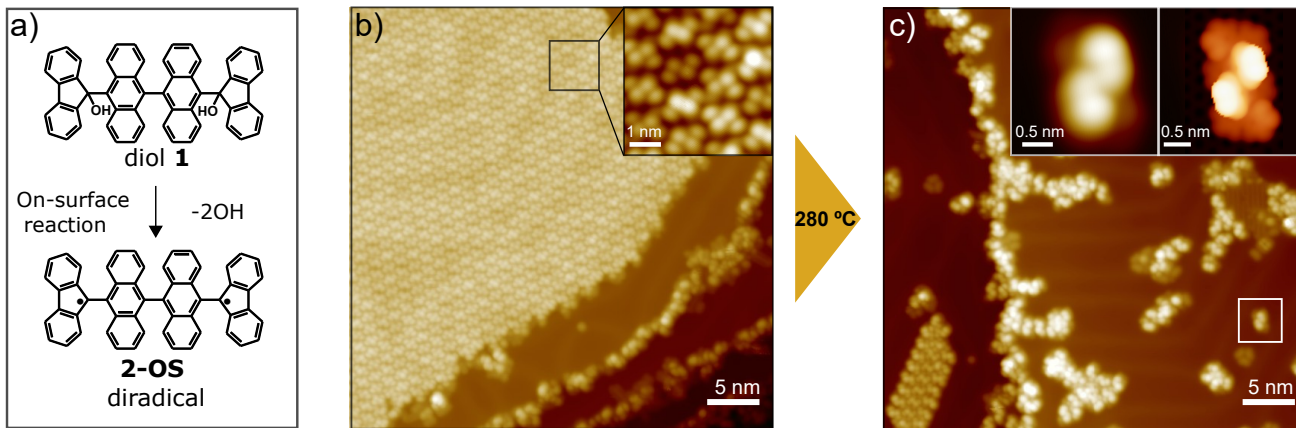


FIG. 1. (a) Schematic representation of the generation of the **2-OS** diradical through dissociation of the OH groups from the diol **1** deposited on the Au(111) substrate. (b) Overview STM constant-current image displaying the typical close-packed domain formed by the molecular precursors when deposited on the Au(111) surface ($V = -1.25$ V; $I = 46$ pA). In the inset, close-packed structure showing the arrangement and the shape of the individual molecules ($V = -1.25$ V; $I = 30$ pA). (c) STM constant-current image recorded after annealing the sample at 280°C ($V = -1.25$ V; $I = 30$ pA). In the inset: left, STM image of a single isolated molecule as found after the annealing ($V = -1.25$ V; $I = 30$ pA); right, DFT charge density calculation of **2-OS** on Au(111).

of either singlet and triplet ground state were detected, suggesting an interplay between the spin coupling and the precise structural conformation of the molecule. In order to unravel the nature of the intramolecular spin coupling in **2-OS**, here we study the magnetic properties of this system on a Au(111) surface at the single-molecule level by means of low-temperature scanning tunneling microscopy (STM) and spectroscopy (STS). Our measurements, combined with mean-field Hubbard (MFH) calculations, reveal the influence of the molecular geometry on the magnetic coupling between the radical centers. Following these findings, we demonstrate the possibility of tuning the spin state of the molecule by modifying the arrangement of its constituent units through mechanical manipulation with the STM tip.

RESULTS AND DISCUSSION

On-surface generation and characterization of 2-OS. Evaporating di- and poly-radicals onto a substrate is known to be particularly challenging, as it easily results in fragmentation due to thermal instability [20, 21]. In order to get intact **2-OS** molecules on a Au(111) surface, we sublimated diol **1**, a stable molecular precursor containing a hydroxyl group (OH) capping each of the two radical centers at the fluorenyl termini, and subsequently induced an on-surface reaction to dissociate the OH groups and generate **2-OS**, as shown schematically in Figure 1a.

The diol **1** was evaporated onto a clean Au(111) surface under ultra-high vacuum (UHV) conditions. Extended close-packed molecular domains were found on the Au surface after the sublimation, as revealed by constant-

current STM images (Figure 1b). A closer look into these structures shows that the constituent molecules appear partially planarized, and display four lobes: the two internal ones can be attributed to the anthracene units and the ones at the ends to the fluorenyl termini. Differential conductance (dI/dV) spectra acquired on the molecules inside the close-packed structures show no fingerprints of magnetism (Figure S7). This is expected as a consequence of the presence of the OH groups of compound **1**, that are not detached upon deposition onto the surface and still passivate the radical centers, preserving the closed-shell structure of the precursor.

The sample was thus annealed with the aim of inducing the C-OH cleavage, in a similar manner to the deoxygenation reaction previously described for epoxyacene derivatives [22]. Figure 1c shows an overview after annealing at 280°C : some close-packed domains of reduced dimensions can still be seen, alongside single isolated molecules, chains and small molecular clusters of several shapes. Individual molecules appear in constant-current STM images as shown in the inset in Figure 1c: they feature two internal brighter lobes, that can be attributed to the anthracene moieties, and darker external features, corresponding to the fluorenyl termini. A more detailed elucidation of the molecular structure with bond resolution is hindered by the non-planarity of the system. However, our DFT simulations of the charge density of **2-OS** on the Au(111) surface (also reported in Figure 1c) is in good agreement with the main features found in the STM topography, confirming our identification of the individual molecules.

An alternative approach for the on-surface formation of **2-OS** consists in inducing the C-OH cleavage by means

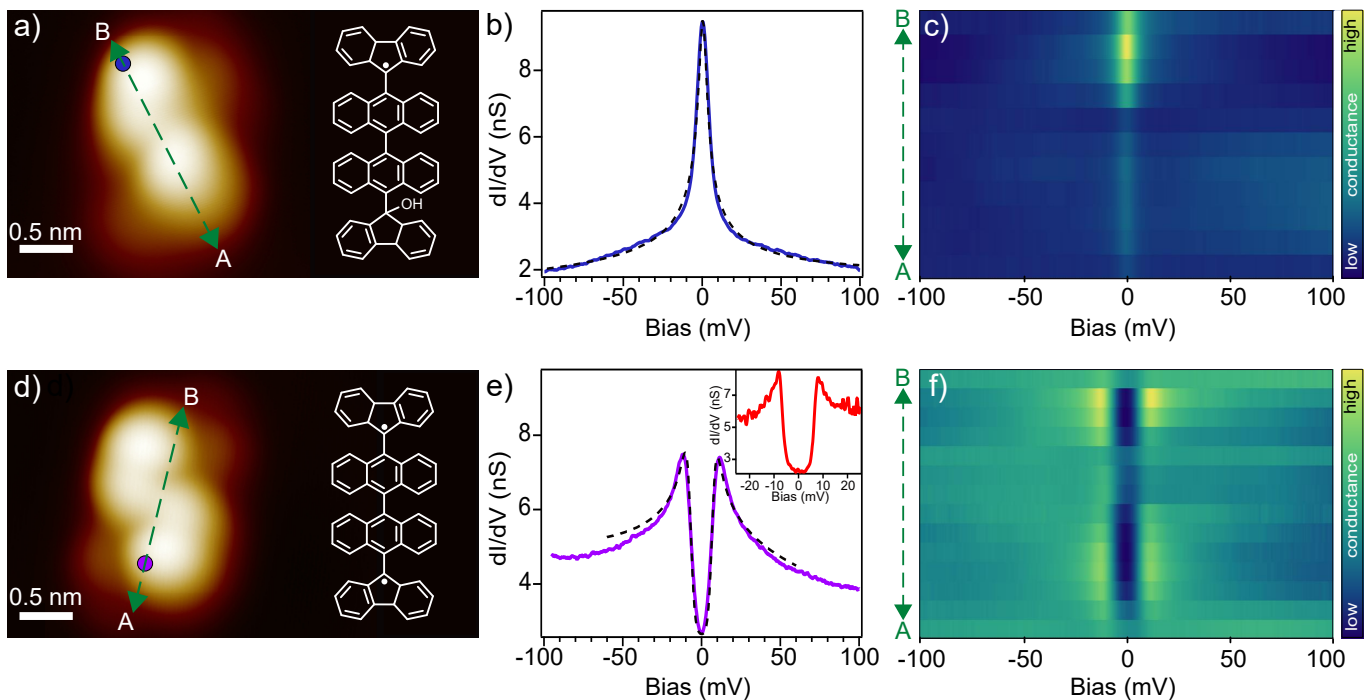


FIG. 2. (a,d) STM constant-current images ($V = -1.25$ V; $I = 30$ pA) of single molecules as found after the on-surface reaction and the corresponding molecular structures, in the two configurations: (a) with a residual OH group, corresponding to a monoradical, and (d) with no OH groups, corresponding to the **2-OS** diradical. (b) dI/dV spectrum taken on the molecule in (a) at the position indicated by the blue circle, displaying a zero-bias resonance, that can be fitted with a Frota function (black dashed line) [23]. (c) dI/dV linescan measured across the molecule in (a) in the direction indicated by the arrow ($V = -200$ mV, $I_{set} = 500$ pA, $V_{mod} = 2$ mV). (e) dI/dV spectrum measured on the molecule in (d) at the position indicated by the purple circle, showing spin excitation steps. The black dashed line represents fits to the data using the perturbative model by Ternes [24], from which an antiferromagnetic exchange $J = 7.3$ meV is obtained. The inset shows a spectrum measured at $T = 1.3$ K, emphasizing the IET gap ($V=30$ mV, $I_{set} = 200$ pA, $V_{mod} = 0.8$ mV). (f) dI/dV line spectra measured across the molecule in (d) in the direction indicated by the arrow ($V = -100$ mV, $I_{set} = 500$ pA, $V_{mod} = 2$ mV).

of a voltage pulse, obtained by placing the tip on top of a molecule and raising the sample positive bias above 1.5 V. As shown in the supplementary information (Figure S8), this procedure allows to remove one or more OH groups in the same molecule or in a neighboring molecule within the assembled domains and molecular clusters, but does not provide isolated molecules over the substrate. Therefore, our further analysis is based on single molecules obtained by annealing the substrate.

Two distinct molecular structures are generally found after the annealing step, corresponding to one or both OH groups detached following the on-surface reaction (Figure 2a,d). The STM constant-current images appear roughly the same in the two cases; nevertheless, scanning tunneling spectroscopy allows the identification of two distinct spin states, that can be related to the two configurations with different numbers of OH groups left.

In a fraction of molecules (around 25% of the single molecules that have been investigated, Figure 2a), the dI/dV spectra display a pronounced zero-bias peak, as depicted in Figure 2b. This feature is well reproduced by a Frota function with $HWHM = 6.1$ meV, and can be

attributed to a Kondo resonance, arising from the screening of a localized spin $S = 1/2$ by the conduction electrons of the metal substrate [3, 23, 25–27]. The dI/dV stacked plot taken along an axis of the molecule (Figure 2c) shows that the Kondo resonance is not spatially homogeneous but significantly more intense in one half of the molecule. We relate this spin state to a monoradical structure in which one OH group persists after the annealing and therefore conclude that the Kondo resonance is associated to the single unpaired electron recovered from the partial OH dissociation.

However, most of the individual molecules found after annealing (Figure 2d) display a distinct low-energy feature consisting of a narrow gap centered at zero-bias, followed by two sharp dI/dV peaks at ± 11 meV, as depicted in Figure 2e. The dI/dV stacked plot in Figure 2f reveals that these features appear distributed all over the molecule, weaker over the center of the molecule but with higher amplitude towards the fluorenyl end-groups. Based on the symmetric position of the dI/dV peaks, we attribute these features to an inelastic excitation of the two exchange-coupled spins at the radical sites [3, 4, 28–

31], confirming that in this case both OH groups have been detached, activating the **2-OS** diradical.

We note that dI/dV spectra exhibit a higher-bias characteristic fall-off, resembling a Kondo resonance superimposed on the gapped spectrum [3, 31]. Furthermore, such Kondo-like feature is absent at zero bias (see STS spectrum recorded at 1.3K in inset in Figure 2e). This indicates that the Kondo-like fluctuations are enabled by inelastic electrons tunneling through the excited state [26, 32] but are absent in the ground state. The spectral shape can be interpreted as caused by the inelastic excitation of a singlet (total spin $S = 0$) ground state into a triplet ($S = 1$) excited state. A model of two antiferromagnetically coupled $1/2$ spins [24] (dashed line in Figure 2e) reproduces well the spectral features, revealing an exchange interaction between the fluorenyl moieties of $J \sim 7.3$ meV. Therefore, we conclude that **2-OS** on a Au(111) surface exhibits a singlet ground state, excluding the previously observed triplet ground state [18], since this would result in a very different spectral line-shape.

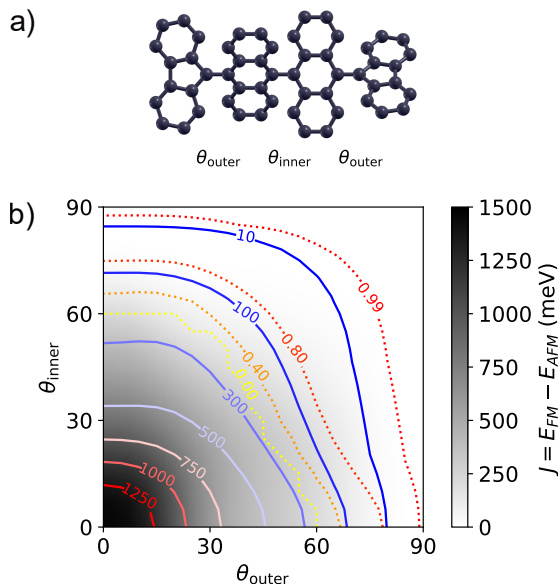


FIG. 3. TB-MFH calculations for the exchange coupling as a function of torsional angles in **2-OS**. (a) Structural model for the **2-OS** carbon backbone with three torsional angles. For simplicity, we fix the two outer angles θ_{outer} to be identical. (b) Using MFH with $U = 3$ eV [33], we solve for the energy difference J between the ferromagnetic (FM) and antiferromagnetic (AFM) solutions as a function of the two torsional angles θ_{outer} and θ_{inner} . The full-line contours represent constant- J while the dashed contours represent the local polarization per radical (sum of the spin density over sites on one half of the molecule) in the AFM solution. The AFM solution is always the one with the lowest electronic energy, but J approaches zero whenever one of the two angles reaches 90° . When $J \gtrsim 200$ meV the AFM solution corresponds to the closed-shell singlet (no local polarization).

Theoretical calculations. To explain the origin of the antiferromagnetic coupling found on the Au substrate, we performed tight-binding mean-field Hubbard (TB-MFH) simulations of the magnetic ground state of **2-OS** in different geometries. Specifically, we calculated the energy of the antiferromagnetic (AFM, the singlet case) spin arrangement with respect to the ferromagnetic (FM, the triplet solution) case, i.e. $J = E_{\text{FM}} - E_{\text{AFM}}$, as a function of the dihedral angles θ_{inner} (between the central anthracenes) and θ_{outer} (between each anthracene and the outer fluorenyl). For simplicity, we assumed the two outer angles to be identical and the individual anthracenes and fluorenyls units to be planar. We considered a single p -orbital per carbon site, locally perpendicular to the backbone unit and constructed the corresponding TB Hamiltonian with SISL [34] using the Slater-Koster parametrization of Rezaei and Phirouznia [35] (see Supplementary Information Section 3.1).

The variation of J as a function of the two torsional angles is depicted in Figure 3b. The AFM solution is always the lowest in energy for any combination of θ_{inner} and θ_{outer} . However, we observe a clear trend in the evolution of J with the conformation: its value is close to 0 when any of the torsional angles approach 90° , but it progressively increases as the angles reduce. This means that the planarization of the molecular structure (i.e. the decrease of the angles between the units) stabilizes the singlet solution, unveiling an increasingly higher AFM exchange coupling. According to the TB-MFH results, the effect is drastic: the open-shell singlet vanishes for angles of just 60° , transforming itself into a (spin non-polarized) closed-shell solution.

The experimental observation of a singlet ground state for **2-OS** on Au(111) is in agreement with the trend obtained in the MFH simulations. The interaction with the flat metal substrate is expected to induce a partial planarization of the molecular units (see the DFT calculation of the adsorption geometry in Supplementary Information Section 3.2), contributing to the stabilization of the AFM order. From TB-MFH results, the FM solution is always less energetically favorable than the AFM one, even for high values of the torsional angles. This apparently contradicts results from previous DFT calculations, which found a triplet ground state in the gas phase, with a triplet-singlet gap of 26 meV [18]. This discrepancy is explained by considering that the value reported by Zeng et al. [18] takes into account also vibrational effects due to temperature. Including these in our DFT simulations, we reproduced the higher stability of the triplet ground state for a gas-phase relaxed molecule (i.e. with both angles $\theta_i \sim 90^\circ$) and at room temperature (shown in Supplementary Information, Section 3.3). At the lower temperature of our experiment, however, vibrational effects do not play a significant role, and DFT qualitatively reproduces the results of the TB-MFH calculations.

In any scenario, all simulation tools agree that decreas-

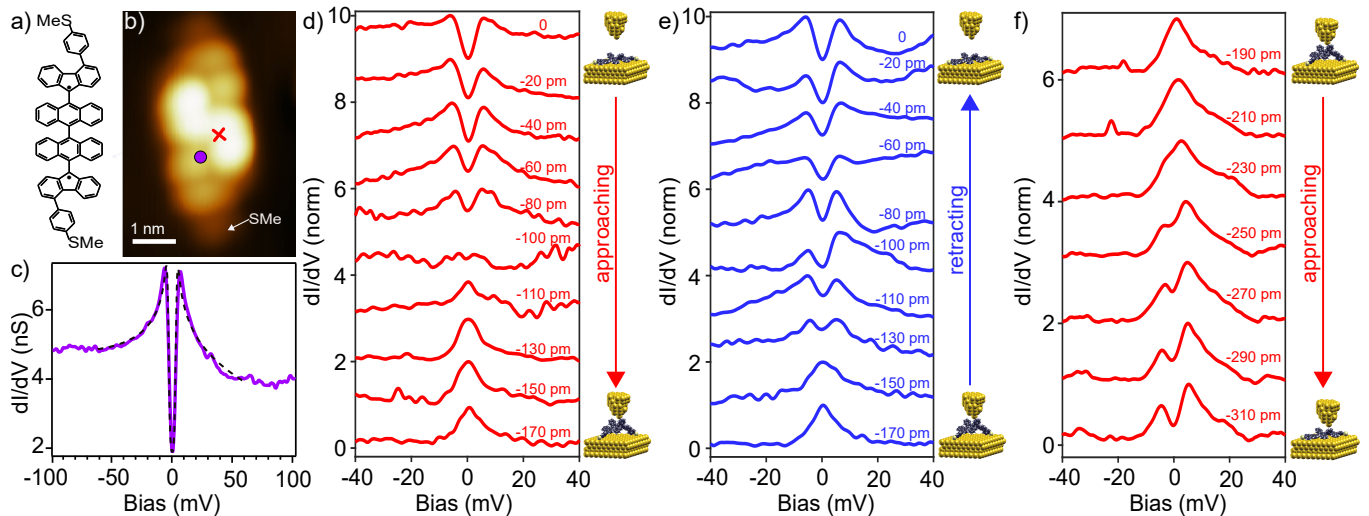


FIG. 4. (a) Chemical model of **SMe-2OS**, the sulfide substituted analogue of **2-OS** synthesized for the manipulation experiment. (b) STM image ($V = -1.25$ V; $I = 30$ pA) of **SMe-2OS**, as obtained after the on-surface generation of the diradical, reported in the Supplementary Information. (c) dI/dV spectrum measured on the molecule at the position indicated by the purple circle in (b), displaying the same IET feature as **2-OS**. The black dashed line is a fit to the data using the perturbative model by Ternes [24], revealing an antiferromagnetic exchange $J = 3$ meV. (d-f) Mechanical manipulation of the spin state of **SMe-2OS**. The STM tip is stabilized on the molecule in the position marked by the red cross in (b) at a starting height (here indicated as 0) determined by the offset parameters $I = 200$ pA and $V = 50$ mV. Then, after opening the feedback loop, dI/dV spectra are measured at different tip heights, in three ranges: (d) while approaching the tip down to 170 pm with respect to the starting position; (e) when retracting back towards the starting position; (f) while continuing approaching to lower tip-sample distances than the ones represented in range (d). On the right of each of the three sets of dI/dV measurements a model represents the process of partially lifting/releasing/pushing the molecule. Spectroscopy parameters: $V_{mod} = 2$ mV, $I_{set} = 200$ pA.

ing the torsional angle of the molecular subunits stabilizes the singlet state. As shown in Figure S11 and S12, this can be explained by the increase in hopping elements across the dihedral angles. These matrix elements primarily enhance kinetic exchange mechanisms, which induce AFM ordering in **2-OS**, while direct Hund's like exchange is expected to be negligible [36, 37]. Following these theoretical results, the controlled modification of the spin interactions should be achievable by tuning the molecular configuration.

Mechanical manipulation of the spin-spin coupling. Motivated by the theoretical predictions indicating a correlation between the geometry of **2-OS** and the exchange coupling J , we explored the possibility of modifying its spin excitation gap and magnetic ground state by controllably manipulating the molecular conformation using the STM tip. We note that the non-planar structure of **2-OS** arises from hindrance among different conjugated units, imposing the persistence of a dihedral angle even on the metal substrate. Consequently, we anticipated that approaching the STM tip towards the central part of the molecule would exert attractive or repulsive forces over these submolecular units, forcing variations of their dihedral angle [38, 39].

However, due to the weak interaction with the surface, **2-OS** molecules were abruptly modified, and fre-

quently displaced towards the STM tip in response to attractive forces (see Figure S9). To overcome this issue, we designed an extended version of the diradical, denoted **SMe-2OS** (Figure 4a), wherein methylthiophenyl moieties were strategically incorporated at each fluorenyl sub-unit. These moieties were chosen since sulfur groups are widely used for anchoring molecules to gold electrodes [40–42].

Similar to the **2-OS** base molecule, we generated the **SMe-2OS** diradical on the Au(111) surface by depositing the corresponding closed-shell precursor containing OH protecting groups at the two radical sites (see structure of diol **10** in Figure S1). In this case, we activated the OH decapping by applying controlled bias pulses over the molecular center, as illustrated in Figure S10.

The STM constant-current image of the resulting **SMe-2OS** molecule, shown in Figure 4b, reveals similar bulky features like in **2-OS** species but with the addition of two smaller bright lobes at each end, attributed to the methylthiophenyl end groups.

The dI/dV spectra measured on **SMe-2OS** (Figure 4c) reproduce similar features as in **2-OS**, namely, IET onsets attributed to singlet-triplet spin excitation, accompanied by a dI/dV decrease characteristic of Kondo fluctuations in the excited state. Therefore, apart from a slightly reduced value of the singlet-triplet gap ~ 3 meV

in **SMe-2OS**), the addition of the edge groups preserves the magnetic ground state of **2-OS**.

To study the evolution of spin interactions in **SMe-2OS** as a function of structural changes, we stabilized the STM tip above the center of the molecule (red cross in Figure 4b) and performed dI/dV measurements while the STM tip was approached to or retracted from the molecule in steps of 10 or 20 pm.

Figure 4d displays spectra measured while approaching the tip 170 pm from the starting position. The width and depth of the excitation gap decreases along the first approaching steps until collapsing into a zero-bias peak at 100 pm. This change can be interpreted as a transition to a new spin state of **SMe-2OS** caused by the structural modification induced by the tip. Approaching the tip towards the molecule is known to induce first attractive forces [43, 44] that here produce a rearrangement of the internal anthracene units into a less planar conformation, as shown in the schematic representation of Figure 4d. As suggested by the theory, an increase in one or both the torsional angles results in the reduction of the intramolecular spin-spin coupling. Therefore, the zero-bias peak observed in the final steps of the approach can be attributed to a Kondo-like feature, emerging when the two spins become non-interacting.

The mechanical manipulation of the spin state of the diradical is reversible (Figure 4e). Retracting the tip back to the starting position restores the initial inelastic spectral features, thus indicating that the molecule is brought back into the original conformation stabilized by the substrate. The reversibility of this process demonstrates that the change in the spectra is due to mechanical modifications rather than to the formation of a tip-molecule bond (and consequent quenching of a spin).

When the STM tip is instead moved further towards the molecule from the closest point in Figure 4d, the antiparallel spin configuration is also restored. Figure 4f shows dI/dV spectra measured while approaching the tip from 190 pm to 310 pm from the starting position in Figure 4d. In this range, the Kondo peak gradually develops a gap with tip approach attributed to the reactivation of an inelastic spin excitation. This indicates that repulsive tip-molecule forces start to play a role and the molecule is pushed back towards the substrate, progressively restoring the torsional angles between the central anthracenes and recovering the antiparallel spin interaction. Curiously, this gap-reopening is smooth, in contrast to the first range of the approach (Figure 4d), where a sudden gap closing took place. This suggests that in the range of pushing, the dihedral angle can be tuned gradually, while during the initial pulling regime, the attractive forces acting at larger distances induce a more sudden structural reorganization. These results demonstrate that the spin-spin coupling in **2-OS** can be tuned by means of mechanical manipulation in a reversible way, confirming the theoretical prediction of a strong interplay between

precise structural conformation and magnetic state.

CONCLUSIONS

In summary, we have demonstrated that the Chichibabin’s hydrocarbon **2-OS** retains its open-shell character on a Au(111) surface with a singlet ground state consisting of two antiparallel aligned spins. Through the cleavage of protecting groups of the deposited diol precursors followed by spatially resolved scanning tunnelling spectroscopy measurements we resolved singlet-triplet excitations at the energy $J \sim 7.3$ meV, thus quantifying their exchange coupling strength. Theoretical MFH simulations found that the substrate-induced partial planarization of **2-OS** favours the antiparallel coupling of the unpaired π electrons, while increasing the torsional angle between the molecular moieties progressively reduces the spin exchange coupling. The ability to tailor magnetic interactions by torsional forces is a promising avenue for the realization of molecule-based sensors. Therefore, we demonstrated this possibility using a **2-OS** molecule functionalized with anchoring end groups, which fix the molecule to the metal while inducing structural modifications with the STM tip. We observed that the spin-spin interaction decreases when the molecule is partially lifted from the substrate (thus acquiring a more orthogonal conformation), and that the initial singlet state can be recovered when bringing it back to a more planar arrangement. The robust singlet ground state found at low temperature contrasts with the triplet ground state found at room temperature [18]. We attributed this temperature dependence to contributions of thermally excited vibrational deformations. Together with the reported high sensitivity of the magnetic ground state of these Chichibabin’s hydrocarbons to mechanical interactions, our results suggest a strong potential of **2-OS** as all-organic spin-cross over material.

METHODS

The (111) surface of a single Au crystal was cleaned by several cycles of sputtering with Ne gas and successive annealing at $T = 600^\circ\text{C}$ under ultrahigh vacuum (UHV) conditions. The precursors of **2-OS** and **SMe-2OS** were prepared in solution following the protocol described in the Supplementary Information (Section 1) and evaporated onto the Au(111) surface held at room temperature. The sublimation of intact precursor molecules can be achieved via fast thermal heating of a silicon wafer loaded with grains of the compound, as well as through a standard Knudsen cell. All the measurements were performed in a custom-made low-temperature STM at 5 K in UHV, with the exception of the dI/dV spectrum in

the inset of Figure 2e, measured in a commercial Joule-Thompson (JT) STM with a base temperature of 1.3 K.

Differential conductance spectra were recorded using a lock-in amplifier with frequency $f = 867.9$ Hz (Figure 2) and $f = 944$ Hz (Figure 4), with the modulation amplitude and current parameters indicated in the text.

The distance-dependent dI/dV measurements reported in Figure 4d-f were performed by stabilizing the tip on top of a molecule with the setpoint parameters indicated in the text and using a custom-built interface to control the tip movement z and simultaneously record the tip movement, the current, the bias and the lock-in signal. The spectra displayed in Figure 4d-f were obtained after subtracting a 3rd order polynomial background adjusted to each spectrum and then normalizing the conductance between the maximum and minimum value, according to the formula $G_{norm}(V) = (G(V) - G_{min}) / (G_{max} - G_{min})$, where $G(V)$ is the differential conductance at bias V , and G_{max} and G_{min} the maximum and minimum value of $G(V)$ respectively.

All STM images and dI/dV spectra were performed with gold-coated tungsten tips. The Figures representing experimental data were prepared using WSxM and SpectraFox softwares [45, 46]. The MFH simulations in Figure 3 and the DFT calculations were realized as explained in the Supplementary Information (Section 3) using the software packages HUBBARD [33], GAUSSIAN [47] and SIESTA [48].

ACKNOWLEDGMENTS

The authors gratefully acknowledge financial support from the Spanish MCIN/AEI/10.13039/501100011033 and the European Regional Development Fund (ERDF) through grants PID2022-140845OB-C61, PID2022-140845OB-C62, PID2020-115406GB-I00, and the Maria de Maeztu Units of Excellence Program CEX2020-001038-M, from the European Union (EU) through the FET-Open project SPRING (863098), the ERC Synergy Grant MolDAM (951519), the ERC-AdG CONSPIRA (101097693), and from the Xunta de Galicia (Centro singular de investigación de Galicia accreditation 2019-2022, ED431G 2019/03 and Oportunus Program). F.R.-L. acknowledges funding by the Spanish Ministerio de Educación y Formación Profesional through the PhD scholarship No. FPU20/03305.

* thomas.frederiksen@ehu.es

† diego.pena@usc.es

‡ ji.pascual@nanogune.eu

[1] de Oteyza, D. G.; Frederiksen, T. Carbon-based nanostructures as a versatile platform for tunable π -

magnetism. *J. Phys.: Condens. Matter* **2022**, *34*, 443001.

- [2] Das, S.; Wu, J. Polycyclic Hydrocarbons with an Open-Shell Ground State. *Phys. Sci. Rev.* **2017**, *2*.
- [3] Li, J.; Sanz, S.; Corso, M.; Choi, D. J.; Peña, D.; Frederiksen, T.; Pascual, J. I. Single spin localization and manipulation in graphene open-shell nanostructures. *Nat. Commun.* **2019**, *10*, 200.
- [4] Mishra, S.; Beyer, D.; Eimre, K.; Ortiz, R.; Fernández-Rossier, J.; Berger, R.; Gröning, O.; Pignedoli, C. A.; Fasel, R.; Feng, X.; Ruffieux, P. Collective All-Carbon Magnetism in Triangulene Dimers. *Angew. Chem. Int. Ed.* **2020**, *59*, 12041–12047.
- [5] Mishra, S.; Beyer, D.; Eimre, K.; Kezilebieke, S.; Berger, R.; Gröning, O.; Pignedoli, C. A.; Müllen, K.; Liljeroth, P.; Ruffieux, P.; Feng, X.; Fasel, R. Topological frustration induces unconventional magnetism in a nanographene. *Nat. Nanotechnol.* **2020**, *15*, 22–28.
- [6] Sugawara, T.; Matsushita, M. M. Spintronics in organic π -electronic systems. *J. Mater. Chem.* **2009**, *19*, 1738–1753.
- [7] Naber, W. J. M.; Faez, S.; van der Wiel, W. G. Organic spintronics. *J. Phys. D: Appl. Phys.* **2007**, *40*, R205–R228.
- [8] Frisenda, R.; Gaudenzi, R.; Franco, C.; Mas-Torrent, M.; Rovira, C.; Veciana, J.; Alcon, I.; Bromley, S. T.; Burzurí, E.; van der Zant, H. S. J. Kondo Effect in a Neutral and Stable All Organic Radical Single Molecule Break Junction. *Nano Lett.* **2015**, *15*, 3109–3114.
- [9] Rajca, A. Organic Diradicals and Polyradicals: From Spin Coupling to Magnetism? *Chem. Rev.* **1994**, *94*, 871–893.
- [10] Lehmann, J.; Gaita-Ariño, A.; Coronado, E.; Loss, D. Quantum computing with molecular spin systems. *J. Mater. Chem.* **2009**, *19*, 1672–1677.
- [11] Sanvito, S. Molecular spintronics. *Chem. Soc. Rev.* **2011**, *40*, 3336–3355.
- [12] Shil, S.; Bhattacharya, D.; Misra, A.; Klein, D. J. A high-spin organic diradical as a spin filter. *Phys. Chem. Chem. Phys.* **2015**, *17*, 23378–23383.
- [13] Fukuda, K.; Nagami, T.; Fujiyoshi, J.-y.; Nakano, M. Interplay between Open-Shell Character, Aromaticity, and Second Hyperpolarizabilities in Indenofluorenes. *J. Phys. Chem. A* **2015**, *119*, 10620–10627.
- [14] Lombardi, F.; Ma, J.; Alexandropoulos, D. I.; Komber, H.; Liu, J.; Myers, W. K.; Feng, X.; Bogani, L. Synthetic tuning of the quantum properties of open-shell radicaloids. *Chem* **2021**, *7*, 1363–1378.
- [15] Dong, S.; Li, Z. Recent progress in open-shell organic conjugated materials and their aggregated states. *J. Mater. Chem. C* **2022**, *10*, 2431–2449.
- [16] Popp, F.; Bickelhaupt, F.; Maclean, C. The electronic structure of chichibabin’s hydrocarbon. *Chem. Phys. Lett.* **1978**, *55*, 327–330.
- [17] Montgomery, L. K.; Huffman, J. C.; Jurczak, E. A.; Grendze, M. P. The molecular structures of Thiele’s and Chichibabin’s hydrocarbons. *J. Am. Chem. Soc.* **1986**, *108*, 6004–6011.
- [18] Zeng, Z.; Sung, Y. M.; Bao, N.; Tan, D.; Lee, R.; Zafra, J. L.; Lee, B. S.; Ishida, M.; Ding, J.; López Navarrete, J. T.; Li, Y.; Zeng, W.; Kim, D.; Huang, K.-W.; Webster, R. D.; Casado, J.; Wu, J. Stable Tetrabenzo-Chichibabin’s Hydrocarbons: Tunable Ground State and Unusual Transition between Their Closed-Shell and

- Open-Shell Resonance Forms. *J. Am. Chem. Soc.* **2012**, *134*, 14513–14525.
- [19] Baum, T. Y.; Fernández, S.; Peña, D.; van der Zant, H. S. J. Magnetic Fingerprints in an All-Organic Radical Molecular Break Junction. *Nano Lett.* **2022**, *22*, 8086–8092.
- [20] Huang, Z.; Zhang, Y.; He, Y.; Song, H.; Yin, C.; Wu, K. A chemist’s overview of surface electron spins. *Chem. Soc. Rev.* **2017**, *46*, 1955–1976.
- [21] Jungthoerfer, T.; Gallagher, N. M.; Kolanji, K.; Giangristostomi, E.; Ovsyannikov, R.; Chassé, T.; Baumgarten, M.; Rajca, A.; Calzolari, A.; Casu, M. B. Challenges in Controlled Thermal Deposition of Organic Diradicals. *Chem. Mater.* **2021**, *33*, 2019–2028.
- [22] Eisenhut, F.; Kühne, T.; García, F.; Fernández, S.; Guitián, E.; Pérez, D.; Trinquier, G.; Cuniberti, G.; Joachim, C.; Peña, D.; Moresco, F. Dodecacene Generated on Surface: Reopening of the Energy Gap. *ACS Nano* **2020**, *14*, 1011–1017.
- [23] Frota, H. O. Shape of the Kondo resonance. *Phys. Rev. B* **1992**, *45*, 1096–1099.
- [24] Ternes, M. Spin Excitations and Correlations in Scanning Tunneling Spectroscopy. *New J. Phys.* **2015**, *17*, 063016.
- [25] Kondo, J. Resistance Minimum in Dilute Magnetic Alloys. *Progr. Theor. Phys.* **1964**, *32*, 37–49.
- [26] Ternes, M.; Heinrich, A. J.; Schneider, W.-D. Spectroscopic manifestations of the Kondo effect on single adatoms. *J. Phys.: Condens. Matter* **2008**, *21*, 053001.
- [27] Li, J.; Sanz, S.; Castro-Esteban, J.; Vilas-Varela, M.; Friedrich, N.; Frederiksen, T.; Peña, D.; Pascual, J. I. Uncovering the Triplet Ground State of Triangular Graphene Nanoflakes Engineered with Atomic Precision on a Metal Surface. *Phys. Rev. Lett.* **2020**, *124*, 177201.
- [28] Hirjibehedin, C. F.; Lutz, C. P.; Heinrich, A. J. Spin Coupling in Engineered Atomic Structures. *Science* **2006**, *312*, 1021–1024.
- [29] Hieulle, J.; Castro, S.; Friedrich, N.; Vegliante, A.; Lara, F. R.; Sanz, S.; Rey, D.; Corso, M.; Frederiksen, T.; Pascual, J. I.; Peña, D. On-Surface Synthesis and Collective Spin Excitations of a Triangulene-Based Nanostar. *Angew. Chem. Int. Ed.* **2021**, *60*, 25224–25229.
- [30] Ortiz, R.; Fernández-Rossier, J. Probing local moments in nanographenes with electron tunneling spectroscopy. *Progr. Surf. Sci.* **2020**, *95*, 100595.
- [31] Hieulle, J.; Garcia Fernandez, C.; Friedrich, N.; Vegliante, A.; Sanz, S.; Sánchez-Portal, D.; Haley, M. M.; Casado, J.; Frederiksen, T.; Pascual, J. I. From Solution to Surface: Persistence of the Diradical Character of a Diindenoanthracene Derivative on a Metallic Substrate. *J. Phys. Chem. Lett.* **2023**, *14*, 11506–11512.
- [32] Paaske, J.; Rosch, A.; Wölfle, P.; Mason, N.; Marcus, C. M.; Nygård, J. Non-equilibrium singlet–triplet Kondo effect in carbon nanotubes. *Nat. Phys.* **2006**, *2*, 460–464.
- [33] Sanz Wuhl, S.; Papior, N.; Brandbyge, M.; Frederiksen, T. hubbard: v0.4.1. 2023; <https://doi.org/10.5281/zenodo.4748765>.
- [34] Papior, N. sisl: v0.14.4.dev46+g8754d4f5. 2023; <https://doi.org/10.5281/zenodo.597181>.
- [35] Rezaei, H.; Phirouznia, A. Modified spin-orbit couplings in uniaxially strained graphene. *Eur. Phys. J. B* **2018**, *91*, 295.
- [36] Jacob, D.; Fernández-Rossier, J. Theory of intermolecular exchange in coupled spin- $\frac{1}{2}$ nanographenes. *Phys. Rev. B* **2022**, *106*, 205405.
- [37] Yu, H.; Heine, T. Magnetic Coupling Control in Triangulene Dimers. *J. Am. Chem. Soc.* **2023**, *145*, 19303–19311.
- [38] Heinrich, B. W.; Ehlert, C.; Hatter, N.; Braun, L.; Lotze, C.; Saalfrank, P.; Franke, K. J. Control of Oxidation and Spin State in a Single-Molecule Junction. *ACS Nano* **2018**, *12*, 3172–3177.
- [39] Vaxevani, K.; Li, J.; Trivini, S.; Ortuzar, J.; Longo, D.; Wang, D.; Pascual, J. I. Extending the Spin Excitation Lifetime of a Magnetic Molecule on a Proximitized Superconductor. *Nano Lett.* **2022**, *22*, 6075–6082.
- [40] Heersche, H. B.; de Groot, Z.; Folk, J. A.; van der Zant, H. S. J.; Romeike, C.; Wegewijs, M. R.; Zobbi, L.; Barreca, D.; Tondello, E.; Cornia, A. Electron Transport through Single Mn₁₂ Molecular Magnets. *Phys. Rev. Lett.* **2006**, *96*, 206801.
- [41] Naghibi, S.; Sangtarash, S.; Kumar, V. J.; Wu, J.-Z.; Judd, M. M.; Qiao, X.; Gorenskaia, E.; Higgins, S. J.; Cox, N.; Nichols, R. J.; Sadeghi, H.; Low, P. J.; Vezoli, A. Redox-Addressable Single-Molecule Junctions Incorporating a Persistent Organic Radical. *Angew. Chem. Int. Ed.* **2022**, *61*, e202116985.
- [42] Lokamani, M.; Kilibarda, F.; Günther, F.; Kelling, J.; Strobel, A.; Zahn, P.; Juckeland, G.; Gothelf, K. V.; Scheer, E.; Gemming, S.; Erbe, A. Stretch Evolution of Electronic Coupling of the Thiophenyl Anchoring Group with Gold in Mechanically Controllable Break Junctions. *J. Phys. Chem. Lett.* **2023**, *14*, 5709–5717.
- [43] Farinacci, L.; Ahmadi, G.; Reecht, G.; Ruby, M.; Bogdanoff, N.; Peters, O.; Heinrich, B. W.; von Oppen, F.; Franke, K. J. Tuning the Coupling of an Individual Magnetic Impurity to a Superconductor: Quantum Phase Transition and Transport. *Phys. Rev. Lett.* **2018**, *121*, 196803.
- [44] Trivini, S.; Ortuzar, J.; Vaxevani, K.; Li, J.; Bergeret, F. S.; Casalilla, M. A.; Pascual, J. I. Cooper Pair Excitation Mediated by a Molecular Quantum Spin on a Superconducting Proximitized Gold Film. *Phys. Rev. Lett.* **2023**, *130*, 136004.
- [45] Horcas, I.; Fernández, R.; Gómez-Rodríguez, J. M.; Colchero, J.; Gómez-Herrero, J.; Baro, A. M. WSXM: A software for scanning probe microscopy and a tool for nanotechnology. *Rev. Sci. Instrum.* **2007**, *78*, 013705.
- [46] Ruby, M. SpectraFox: A free open-source data management and analysis tool for scanning probe microscopy and spectroscopy. *SoftwareX* **2016**, *5*, 31–36.
- [47] Frisch, M. J.; Trucks, G. W.; Schlegel, H. B.; Scuseria, G. E.; Robb, M. A.; Cheeseman, J. R.; Scalmani, G.; Barone, V.; Petersson, G. A.; Nakatsuji, H.; Li, X.; Caricato, M.; Marenich, A. V.; Bloino, J.; Janesko, B. G.; Gomperts, R.; Mennucci, B.; Hratchian, H. P.; Ortiz, J. V.; Izmaylov, A. F. et al. Gaussian 16 Revision C.01. 2016; Gaussian Inc. Wallingford CT.
- [48] Soler, J. M.; Artacho, E.; Gale, J. D.; García, A.; Junquera, J.; Ordejón, P.; Sánchez-Portal, D. The SIESTA method for ab initio order-N materials simulation. *J. Phys.: Condens. Matter* **2002**, *14*, 2745–2779.

Supplementary Information:

**Tuning the Spin Interaction in Non-planar Organic Diradicals
Through Mechanical Manipulation**

Alessio Vegliante,¹ Saleta Fernandez,² Ricardo Ortiz,³ Manuel Vilas-Varela,²
Thomas Baum,⁴ Niklas Friedrich,¹ Francisco Romero Lara,¹ Andrea Aguirre,⁵
Katerina Vaxevani,¹ Dongfei Wang,¹ Carlos García,³ Herre S. J. van der
Zant,⁴ Thomas Frederiksen,^{3,6} Diego Peña,² and Jose Ignacio Pascual^{1,6}

¹*CIC nanoGUNE-BRTA, 20018 Donostia-San Sebastián, Spain*

²*Centro Singular de Investigación en Química Biolóxica e Materiais
Moleculares (CiQUS) and Departamento de Química Orgánica,
Universidade de Santiago de Compostela 15782-Santiago de Compostela (Spain)*

³*Donostia International Physics Center (DIPC),
20018 Donostia-San Sebastián, Spain*

⁴*Kavli Institute of Nanoscience, Delft University of Technology, 2628 Delft, The Netherlands*

⁵*Centro de Física de Materiales CSIC/UPV-EHU-Materials Physics Center,
20018 Donostia-San Sebastián, Spain*

⁶*IKERBASQUE, Basque Foundation for Science, 48013 Bilbao, Spain*

1. SYNTHETIC DETAILS

1.1. General methods for the synthesis in solution

All the reactions were carried out under argon using oven-dried glassware. CH_2Cl_2 and tetrahydrofuran (THF) were dried using a MBraun SPS-800 Solvent Purification System. Finely powdered SnCl_2 was purchased from Sigma-Aldrich, weighed and stored in a glove-box. Other commercial reagents were purchased from ABCR GmbH, Sigma-Aldrich or Acros Organics, and were used without further purification. Deuterated solvents were purchased from Acros Organics. TLC was performed on Merck silica gel 60 F254 and chromatograms were visualized with UV light (254 and 365 nm) and/or stained with Hanessian's stain. Column chromatography was performed on Merck silica gel 60 (ASTM 230-400 mesh). ^1H and ^{13}C NMR spectra were recorded at 300 and 75 MHz (Varian Mercury-300 instrument) or 500 and 125 MHz (Varian Inova 500 or Bruker 500) respectively. APCI high resolution mass spectra were obtained on a Bruker Microtof. The synthesis of precursor **1** was performed following a known procedure [1], while precursor **10** was obtained by a similar protocol shown in Scheme 1.

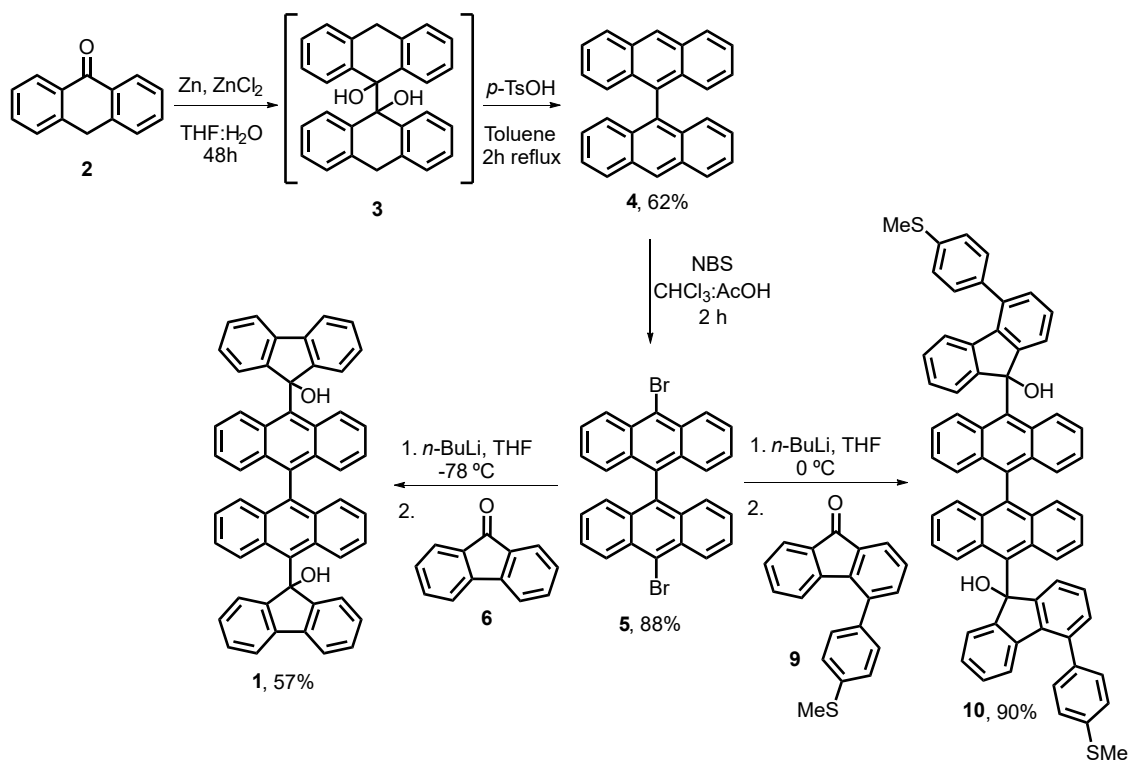
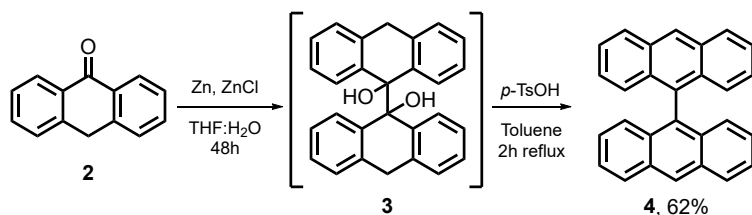


FIG. S1: Scheme 1. Synthesis of molecular precursors **1** and **10**.

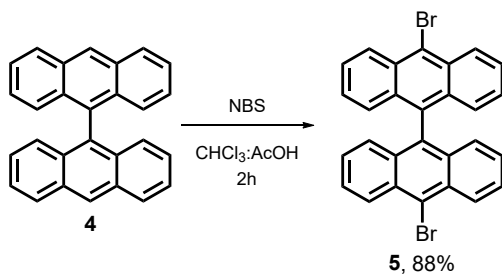
1.2. Synthesis of 9,9'-bianthracene (4)



9-Anthrone (**2**, 2.0 g, 10.3 mmol) was added over a suspension of Zn (3.34 g, 52 mmol) and ZnCl₂ (2.8 g, 20.6 mmol) in THF:H₂O (7: 3, 20mL) and the resulting mixture was stirred at room temperature during 48 h. Then, CH₂Cl₂ (20 mL) and H₂O (20 mL) were added, the phases were separated, and the aqueous phase was extracted with CH₂Cl₂ (2x10 mL). The combined organic phases were dried over MgSO₄, filtered, and concentrated under reduced pressure. The resulting residue was dissolved in toluene (15 mL) and added a catalytic amount of *p*-TsOH, the mixture was refluxed for 2h. The solvent was evaporated, and the residue obtained was purified by column chromatography (SiO₂; hexane: CH₂Cl₂ 4: 1) yielding the product **4** (1.13 g, 62%) as a greenish solid [2].

¹H NMR (300 MHz, CDCl₃) δ: 8.68 (s, 1H), 8.17-8.14 (d, *J* = 8.6 Hz, 2H), 7.47-7.42 (t, *J* = 7.5 Hz, 2H), 7.17-7.06 (dt, *J* = 16.2, 8.7 Hz, 4H) ppm.

1.3. Synthesis of 10,10'-bromo-9,9'-bianthracene (5)



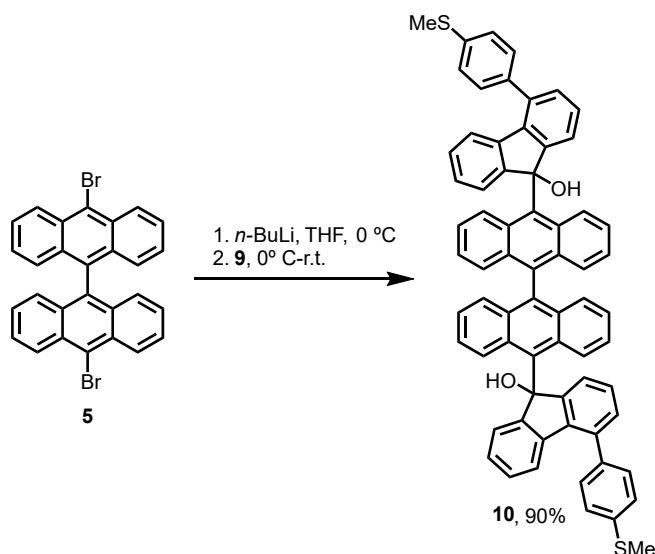
A mixture of compound **4** (1.13 g, 3.2 mmol) and NBS (1.42g, 7.97 mmol) in CHCl₃:CH₃CO₂H(6:1) was refluxed for 16 h. The mixture was then allowed to cool down to room temperature, CHCl₃ (40 mL) and H₂O (40 mL) were added, the phases were separated, and the aqueous phase was extracted with CHCl₃ (2x50 mL). The combined organic phases were dried over MgSO₄, filtered, and concentrated under reduced pressure. The resulting residue was purified by column chromatography (SiO₂; hexane: CH₂Cl₂ 4:1) obtaining the product **5** (1.43 g, 88%) as a yellow solid [3].

¹H NMR (300 MHz, CDCl₃) δ: 8.74-8.71 (d, *J* = 8.9 Hz, 1H), 7.63-7.58 (m, 1H), 7.23-7.18 (dd, *J* = 8.6, 6.6 Hz, 1H), 7.11-7.08 (d, *J* = 8.8 Hz, 1H) ppm.

yellow solid.

^1H NMR (300 MHz, CDCl_3) δ : 7.64 (q, $J = 5.0$ Hz, 2H), 7.36 (s, 4H), 7.29 (d, $J = 4.7$ Hz, 2H), 7.19 (dd, $J = 5.5, 3.2$ Hz, 2H), 6.88 – 6.83 (m, 1H), 2.57 (s, 3H). ^{13}C NMR (75 MHz, CDCl_3) δ : 193.8 (CO), 144.5 (C), 141.1 (C), 138.9 (C), 137.7 (C), 136.8 (CH), 136.0 (C), 134.8 (C), 134.4 (CH), 129.3 (CH), 128.8 (CH), 128.7 (CH), 126.4 (CH), 124.2 (CH), 123.3 (CH), 123.2 (CH), 15.6 (CH_3).ppm.HRMS (APCI): $\text{C}_{20}\text{H}_{15}\text{OS}$; calculated: 303.0838, found: 303.0839.

1.6. Synthesis of diol **10**, precursor of SMe-2OS



In a round bottom flask, compound **5** (77 mg, 0.15 mmol) and dry THF (5 mL) were added under argon atmosphere. The solution was cooled to 0 °C and *n*-BuLi solution (2.5 M in hexane, 132 μL , 0.33 mmol) was dropwise added. The mixture was stirred for 10 min at 0 °C and then fluorenone **9** (100 mg, 0.38 mmol) in THF (1 mL) was added. The solution was slowly warmed to room temperature and stirred for 16h. Then water (10 mL) was added, and the mixture was extracted with EtOAc (3x5 mL). The organic layer was dried over anhydrous MgSO_4 and filtered. The solvent was removed under reduced pressure and the residue was purified by column chromatography (SiO_2 ; Hexanes: CH_2Cl_2 1:1 to 1:9) affording product **10** (120 mg, 90%) as a greenish solid.

^1H NMR (300 MHz, CDCl_3) δ : 9.86 (d, $J = 9.3$ Hz, 2H), 7.57 – 7.34 (m, 14H), 7.24 – 7.17 (m, 4H), 7.17 – 7.07 (m, 12H), 6.96 (d, $J = 8.6$ Hz, 2H), 6.81 (t, $J = 7.2$ Hz, 2H), 6.72 (t, $J = 7.8$ Hz, 2H), 2.80 (s, 2H), 2.56 (s, 6H) ppm. ^{13}C NMR (300 MHz, CDCl_3) δ 153.4 (C), 152.9 (C), 138.8 (C), 138.4 (C), 137.4 (C), 135.8 (C), 135.7 (C), 134.1 (C), 132.7 (C), 132.0 (C), 131.5 (C), 131.4 (CH), 129.8 (CH), 129.1 (C), 128.9 (CH), 128.8 (CH), 128.7 (CH), 128.6 (CH), 128.5 (CH), 127.8 (CH), 127.3 (CH), 126.6 (CH), 126.3 (CH), 125.2 (CH), 125.0 (CH), 124.8 (CH), 124.6 (CH), 124.1 (CH), 124.0 (CH), 86.8 (C), 15.8 (CH_3) ppm. HRMS (APCI): $\text{C}_{68}\text{H}_{46}\text{O}_2\text{S}_2$; calculated: 958.2939, found: 958.2944.

1.7. Spectroscopic data

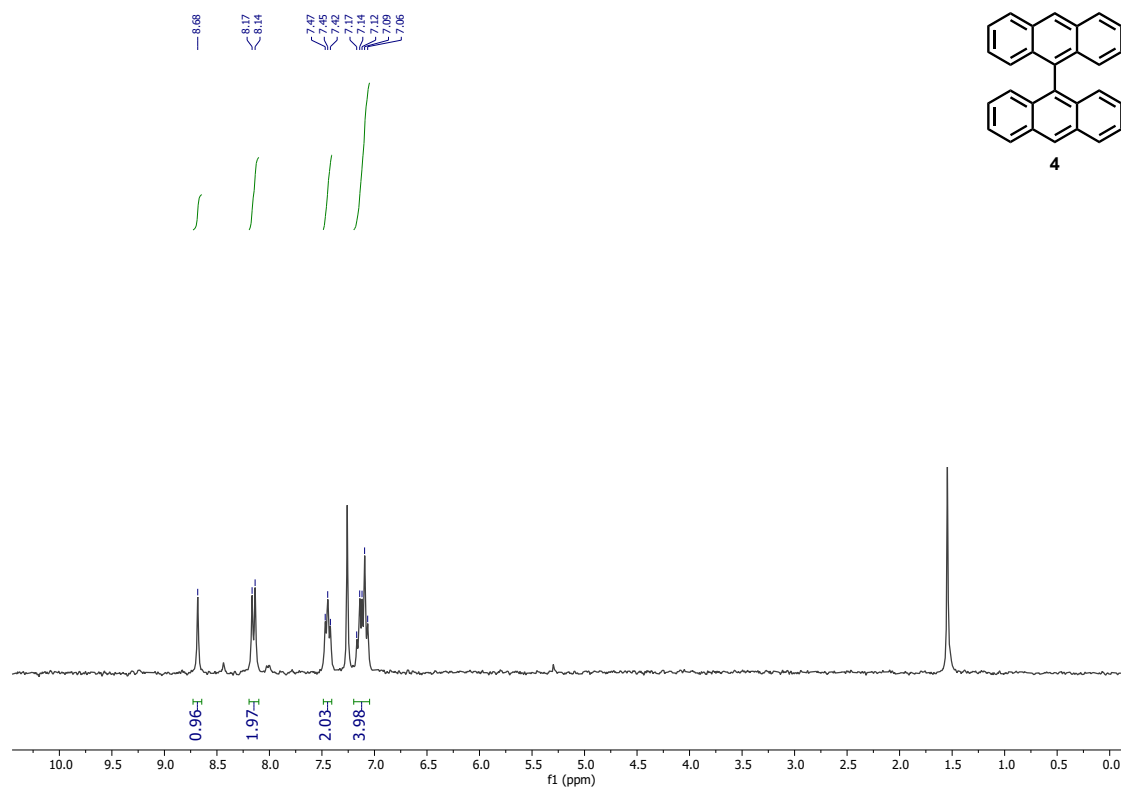


FIG. S2: ^1H NMR (300 MHz, CDCl_3) spectrum of 9,9'-bianthracene (4).

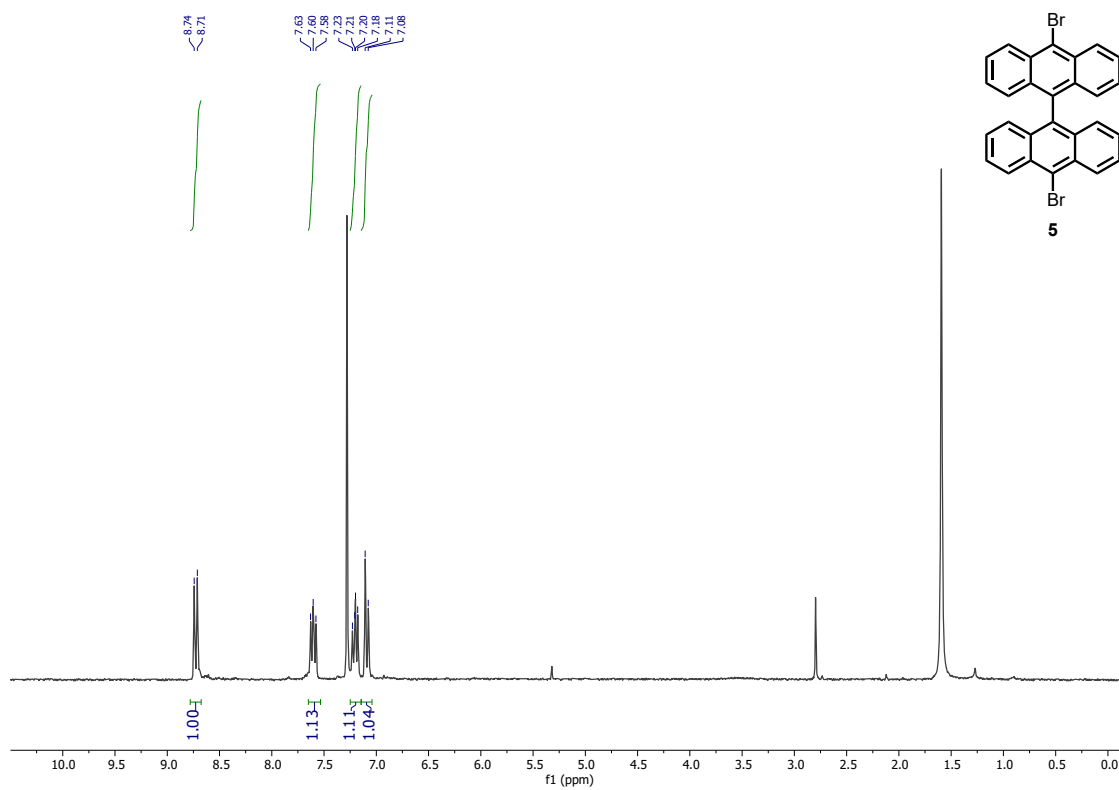


FIG. S3: $^1\text{H NMR}$ (300 MHz, CDCl_3) spectrum of 10,10'-dibromo-9,9'-bianthracene (**5**).

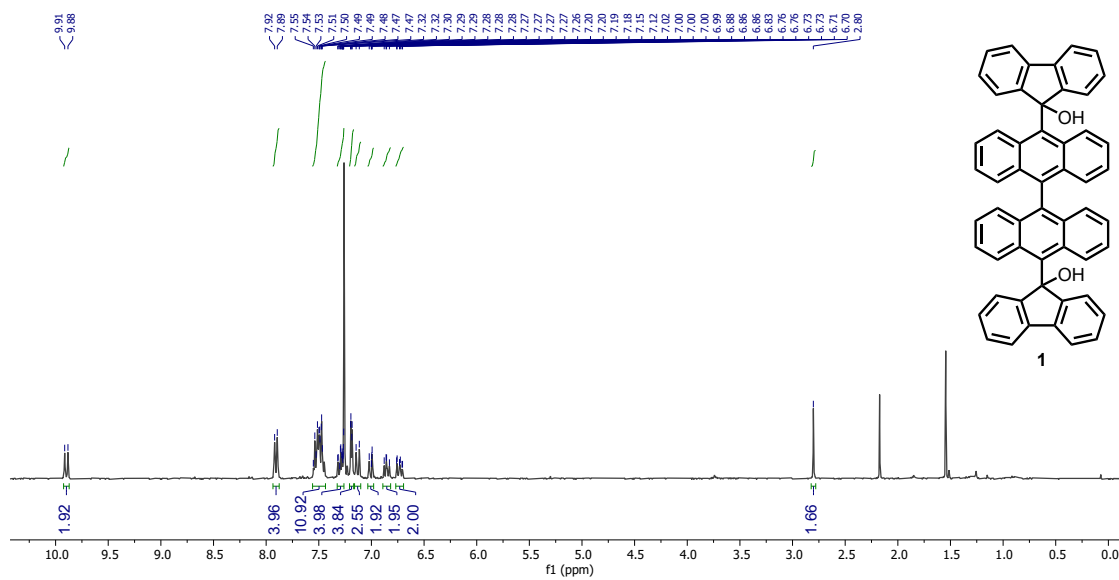


FIG. S4: $^1\text{H NMR}$ (300 MHz, CDCl_3) spectrum of precursor **1**.

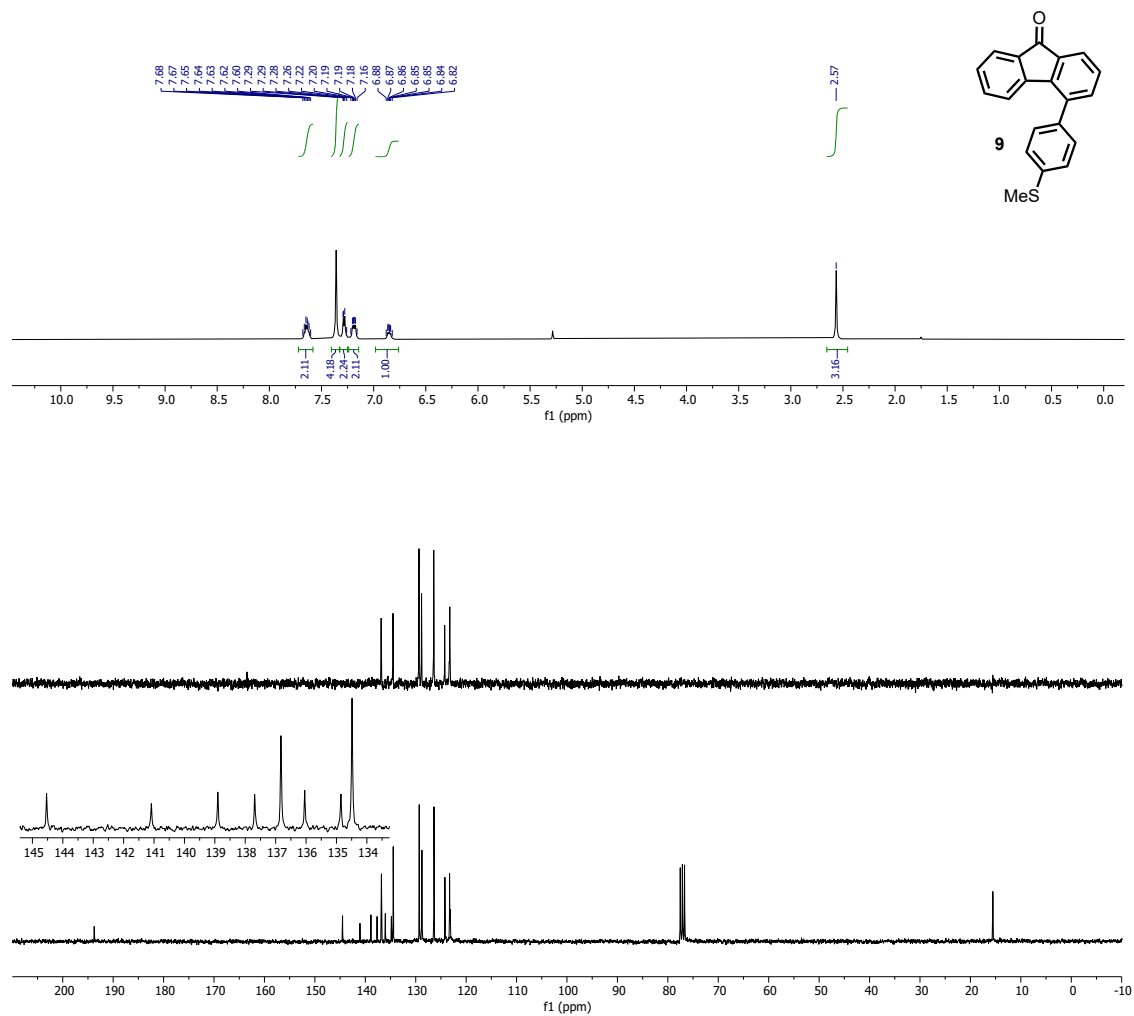


FIG. S5: ^1H and ^{13}C NMR (300 MHz, CDCl_3) spectra of 4-(4-(methylthio)phenyl)-9H-fluoren-9-one (**9**).

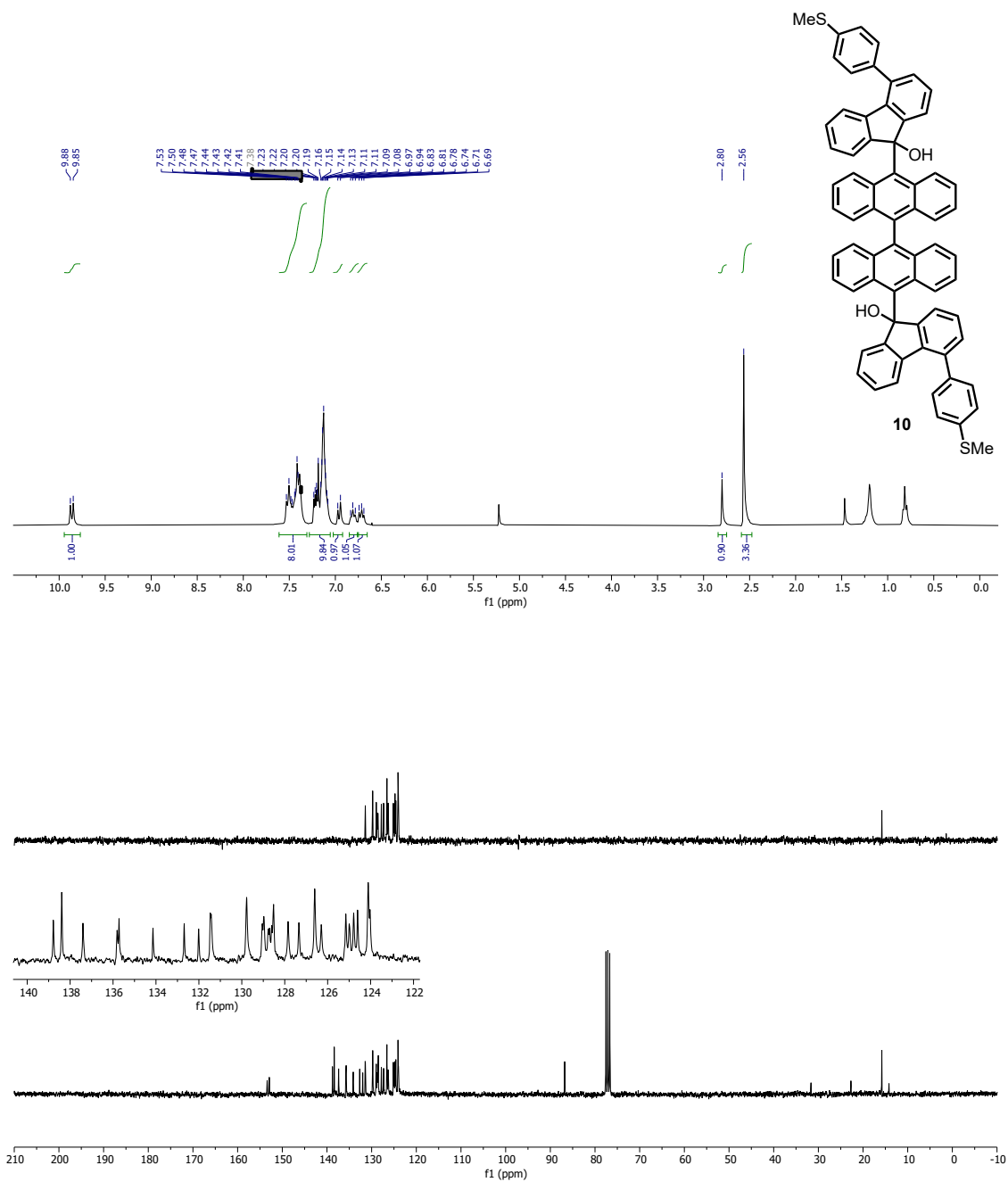


FIG. S6: ¹H and ¹³C NMR (300 MHz, CDCl₃) spectra of diol **10**.

2. COMPLEMENTARY EXPERIMENTAL DATA

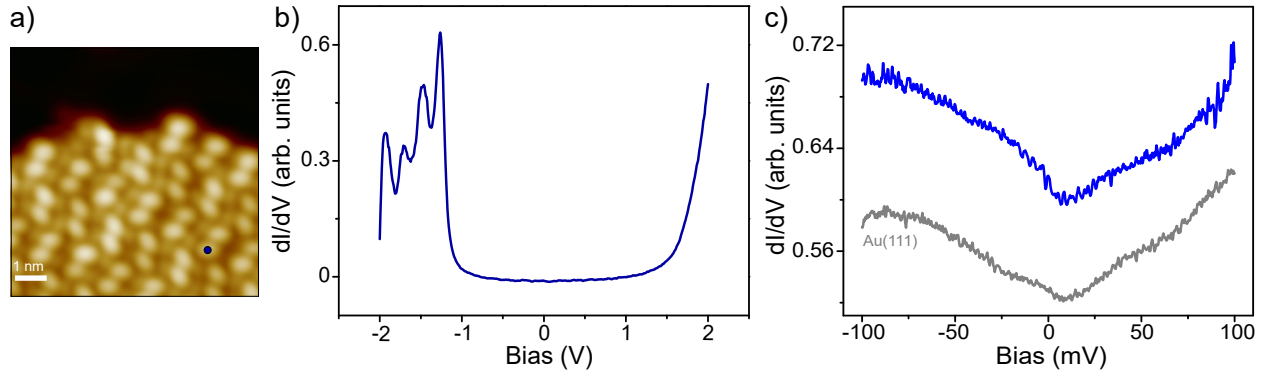


FIG. S7: Long- and short-range dI/dV spectra measured on the molecular precursor (diol **1**) inside a close-packed island. (a) STM constant-current image of a close-packed domain formed by the molecular precursors deposited on the Au(111) surface ($V = 1$ V; $I = 30$ pA). (b) Long-range dI/dV spectrum acquired in the position indicated by the blue circle in (a). Parameters: $V_{mod} = 10$ mV, $I_{set} = 500$ pA. (c) Short-range spectrum acquired on a molecule in the close-packed domain (blue curve), showing no magnetic fingerprints, due to the presence of passivating OH groups in diol **1**. Grey curve corresponds to a reference spectrum acquired on the bare Au(111) surface. Parameters: $V_{mod} = 2$ mV, $I_{set} = 400$ pA.

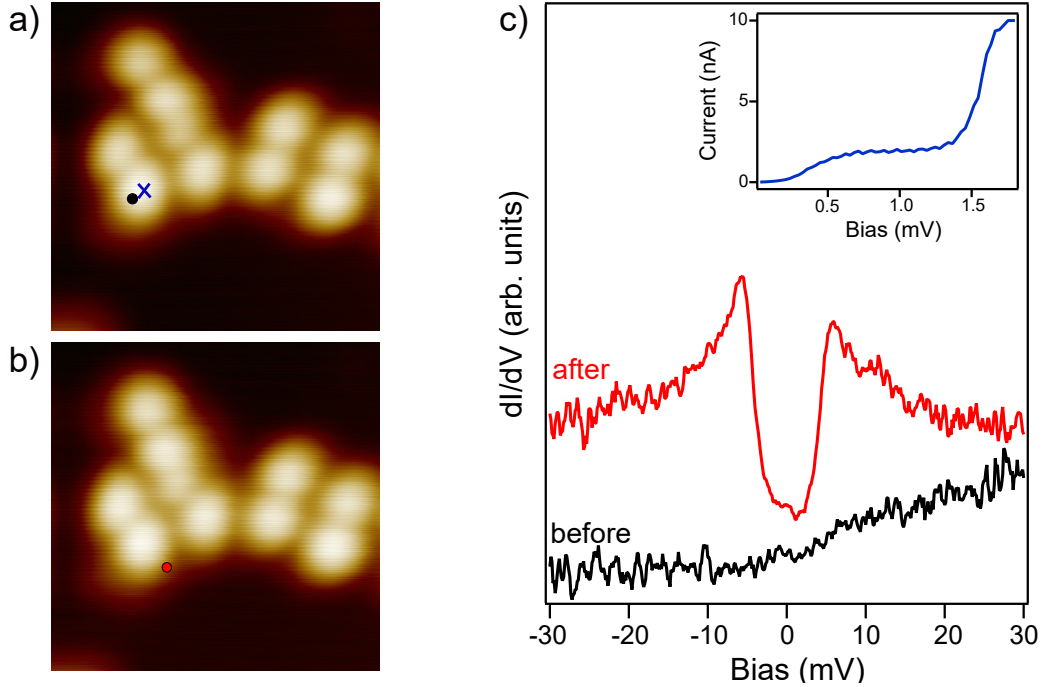


FIG. S8: On-surface generation of **2-OS** by electron-induced C-OH cleavage. (a) Constant-current STM image of a small island of precursor molecules (diol **1** in Figure S1). The blue cross indicates the position where the tip is stabilized (setpoint: $V = 30$ mV, $I = 10$ pA) before sweeping the bias. (b) Constant-current STM image of the same area after the bias sweep. (c) dI/dV spectra measured before (black) and after (red) the bias sweep from 30 mV to 2 V at the positions indicated in (a,b) by the corresponding circles. The inset shows the variation of the tunneling current during the process. After the bias sweep, the diradical is generated, as clearly demonstrated by the appearance of the IET steps attributed to the two exchange-coupled spins. This experiment was performed at $T = 1.3$ K. Topography parameters: $V = 2$ V; $I = 10$ pA. Spectroscopy parameters: $V_{mod} = 0.8$ mV, $I_{set} = 200$ pA.

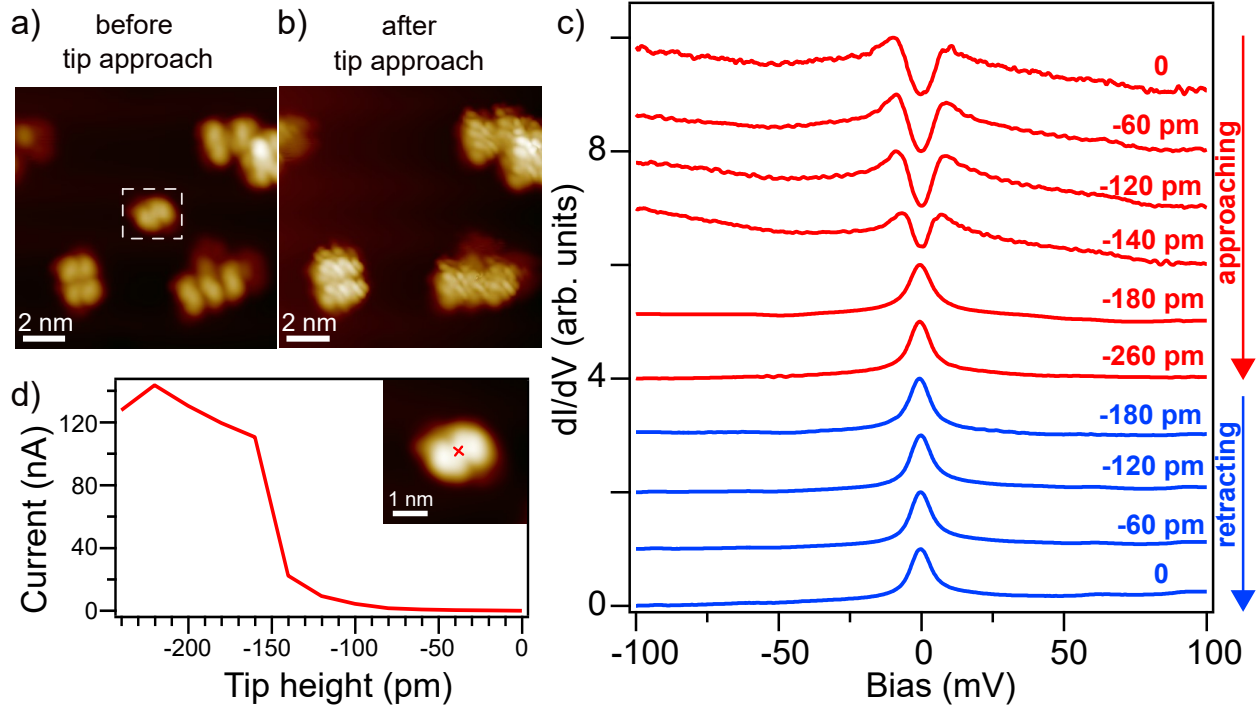


FIG. S9: Manipulation experiments on **2-OS**. (a) Constant-current STM image of the molecule on which the tip approach experiment is performed, as seen before starting the process ($V = -1.25$ V; $I = 30$ pA); (b) Image of the same area after the manipulation, showing that the molecule has been unintentionally picked up by the tip. (c) Stack of normalized dI/dV spectra recorded during the approach-retracting experiment on the **2-OS** molecule. The manipulation procedure is the following: we stabilize the tip above **2-OS**, in the position indicated by the cross in the inset in (d), at a starting height ($z = 0$) determined by a setpoint of $V = 100$ mV and $I = 200$ pA; then we approach towards the molecule in steps of 20 pm, measuring dI/dV spectra at each step, and finally retract back to the starting point. Red curves are recorded during approaching, blue curves during retraction. We can observe the appearance of a Kondo peak and simultaneous disappearance of the IET steps at -180 pm. The Kondo feature persists while retracting the tip back to the starting position: this suggests that the change in the spectral feature is due to the quenching of one of the two radicals upon formation of a tip-molecule contact, as confirmed also by the image recorded at the end of the process (b), which shows that the molecule has been picked up during the process. (d) Current at $V = 100$ mV recorded during the approach experiment presented in panel c). The sharp increase at -150 pm coincides with the change of magnetic fingerprint in the dI/dV spectra. Spectroscopy parameters: $V_{mod} = 2$ mV, $I_{set} = 200$ pA.

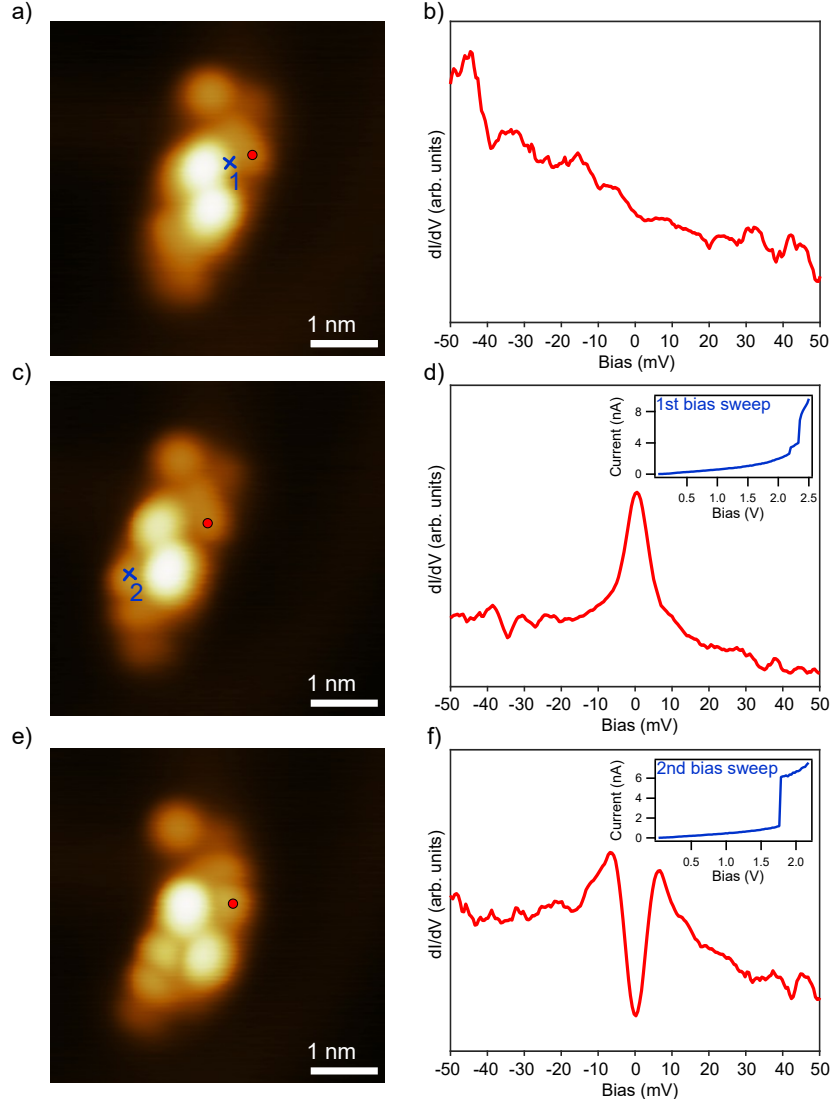


FIG. S10: On-surface generation of **SMe-2OS** by sequential electron-induced C-OH cleavage. (a) Constant-current STM image of the closed-shell precursor (diol **10** in Figure S1) as deposited on the Au(111) surface. (b) Low bias dI/dV spectrum measured at the position indicated by the red circle in (a) before the bias sweep, displaying no magnetic fingerprints, as expected for the closed-shell precursor. (c) Constant-current STM image of the molecule after the first bias sweep. The tip is stabilized in the position indicated by the blue cross in (a) (setpoint: $V = 30$ mV, $I = 10$ pA) before opening the feedback and raising the bias above 30 mV. (d) dI/dV spectrum measured after the first bias sweep in the position indicated by the red circle in (c), showing a Kondo peak that emerges as a consequence of the removal of one OH group. The inset reports the variation of the tunneling current during the bias sweep (from 30 mV to 2.5 V): the sudden jump at 2.3 V indicates the C-OH cleavage. (e) Constant-current STM image of the molecule after the second bias sweep, performed in the position indicated by the blue cross in (c), corresponding to the site where the second OH is located. (f) dI/dV spectrum measured after the second bias sweep at the position marked by the red circle in (e). The inset reports the variation of the current as a function of the bias (ramping from 30 mV to 2.1 V) with a step increase at 1.8V. Now clear IET features appear, indicating the dissociation of the second OH group. Topography parameters: $V = 1$ V; $I = 30$ pA. Spectroscopy parameters: $V_{mod} = 2$ mV, $I_{set} = 500$ pA.

3. COMPLEMENTARY THEORETICAL RESULTS

3.1. MF-Hubbard modeling based on Slater-Koster parametrization

In order to explore the role of the torsion angles of **2-OS** we implemented an effective non-orthogonal tight-binding description based on a Slater-Koster parametrization [4]. Our model considers a single p orbital per carbon site perpendicular to the anthracene (or fluorenyl) plane to which the atom belongs.

Consider two local p_z -orbitals i and j , located arbitrarily at positions \mathbf{R}_i and \mathbf{R}_j and rotated by angles φ_i and φ_j (only) around the x axis (oriented along the torsional bond of interest). With $\mathbf{n} = (n_x, n_y, n_z)$ being the unit vector connecting the two orbital centers, and $d = |\mathbf{R}_i - \mathbf{R}_j|$ the distance between them, the effective hopping matrix element in the SK Hamiltonian connecting the basis orbitals can be expressed as

$$t_{ij} = (t_{zz} \cos \varphi_i + t_{yz} \sin \varphi_i) \cos \varphi_j + (t_{yz} \cos \varphi_i + t_{yy} \sin \varphi_i) \sin \varphi_j \quad (1)$$

where

$$t_{yz} = n_y n_z (V_{pp\sigma} - V_{pp\pi}) \quad (2)$$

$$t_{yy} = n_y^2 V_{pp\sigma} + (1 - n_y^2) V_{pp\pi} \quad (3)$$

$$t_{zz} = n_z^2 V_{pp\sigma} + (1 - n_z^2) V_{pp\pi} \quad (4)$$

are expressed in terms of the two-centre SK parameters

$$V_{pp\alpha}(d) = V_{pp\alpha}^0 \exp\left(-\beta_{pp\alpha} \frac{d - d_0}{d_0}\right), \quad \alpha = \sigma, \pi. \quad (5)$$

Similarly, the orbital overlap can be expressed as

$$s_{ij} = (s_{zz} \cos \varphi_i + s_{yz} \sin \varphi_i) \cos \varphi_j + (s_{yz} \cos \varphi_i + s_{yy} \sin \varphi_i) \sin \varphi_j \quad (6)$$

where

$$s_{yz} = n_y n_z (S_{pp\sigma} - S_{pp\pi}) \quad (7)$$

$$s_{yy} = n_y^2 S_{pp\sigma} + (1 - n_y^2) S_{pp\pi} \quad (8)$$

$$s_{zz} = n_z^2 S_{pp\sigma} + (1 - n_z^2) S_{pp\pi} \quad (9)$$

and

$$S_{pp\alpha}(d) = S_{pp\alpha}^0 \exp\left(-\beta_{pp\alpha} \frac{d - d_0}{d_0}\right), \quad \alpha = \sigma, \pi. \quad (10)$$

Following Ref.[5] we chose their parameters for our model:

$$V_{pp\sigma} = 6.20 \text{ eV}, \quad (11)$$

$$V_{pp\pi} = -3.07 \text{ eV}, \quad (12)$$

$$\beta_{pp\sigma} = 1.47, \quad (13)$$

$$\beta_{pp\pi} = 3.104, \quad (14)$$

$$S_{pp\sigma} = -0.140, \quad (15)$$

$$S_{pp\pi} = 0.07, \quad (16)$$

$$\beta'_{pp\sigma} = 0.77, \quad (17)$$

$$\beta'_{pp\pi} = 2.11, \quad (18)$$

$$d_0 = 1.42 \text{ \AA}. \quad (19)$$

Using a custom implementation based on SISL [6], some characteristic hopping matrix elements t_{ij} between fluorenyl and anthracene sites are shown in Figure S11. Similarly, the overlaps s_{ij} are shown in Figure S12.

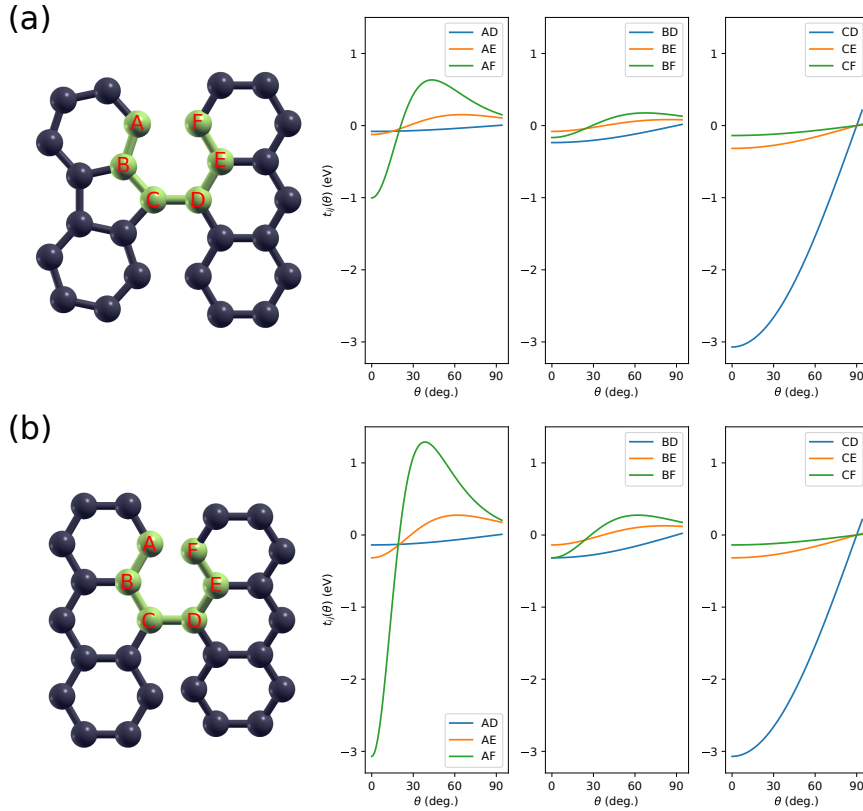


FIG. S11: Selective SK hopping matrix elements t_{ij} between characteristic sites as a function of the torsional angle θ around the C–D bond connecting (a) fluorene and anthracene or (b) two anthracene units.

In addition to this effective one-orbital-per-site SK model, we consider in the main text (Figure 3) also a local onsite Coulomb repulsion U in the mean-field approximation (MF-

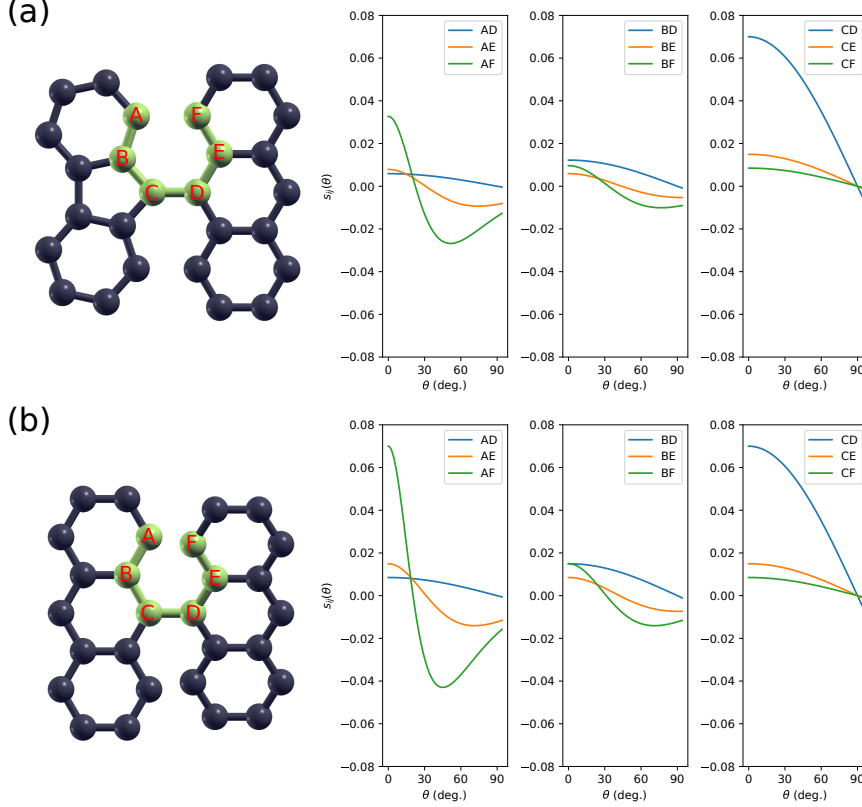


FIG. S12: Selective SK overlap matrix elements s_{ij} between characteristic sites as a function of the torsional angle θ around the C–D bond connecting (a) fluorene and anthracene or (b) two anthracene units.

Hubbard). We solve iteratively for the symmetry-broken solutions corresponding to $S_z = 0$ (AFM or unpolarized) and $S_z = 1$ (FM) using HUBBARD [7].

In addition to this, we also checked the ground state of **2-OS** using CASSCF-NEVPT2 calculations, confirming the stability of the $S_z = 0$ ground state, which is mostly degenerate with the $S_z = 1$ excited state in gas phase.

3.2. DFT study of surface adsorption geometry

In our study, Density Functional Theory (DFT) calculations were executed using SIESTA [8] to understand the interactions between **2-OS** and the metallic surface. We applied the van der Waals density functional formulated by Dion *et al.* [9] with the modified exchange by Klimeš, Bowler and Michaelides [10], to effectively capture the dispersive forces at play. We used a double- ζ basis set for valence-electron wave function expansion, with orbital radii determined by a 100 meV energy shift and core electrons described via norm-conserving Troullier-Martins pseudopotentials. Brillouin zone sampling was conducted with a simple $1 \times 1 \times 1$ k -point grid. The Au(111) surface modeling utilized a 9×9 -repeated, four-layer thick slab, characterized by a 4.08 Å lattice parameter, with an extended basis for the top atomic layer [11] and hydrogen passivation on the bottom layer to mitigate spurious

surface state interactions [12]. The real-space grid was defined by a 300 Ry energy cutoff. Electronic occupations were smeared using a Fermi-Dirac distribution at a 300 K electronic temperature. Our self-consistency cycle criteria included convergence thresholds of less than 10^{-4} for the density and less than 1 meV for the Hamiltonian matrix elements, respectively. Geometry optimizations for the **2-OS** molecule and the top three layers of the Au(111) slab were performed using the conjugate gradient method, ensuring forces were below 0.01 eV/Å. The adsorption geometry is shown in Fig. S13. In this adsorption configuration we could not stabilize the antiferromagnetic spin state of the gas-phase molecule, but it was recovered by increasing the molecule-surface distance by 0.5 Å or more. The image shown in the inset of Figure 1c (main text) was obtained from the calculated charge density using the WSxM software [13].

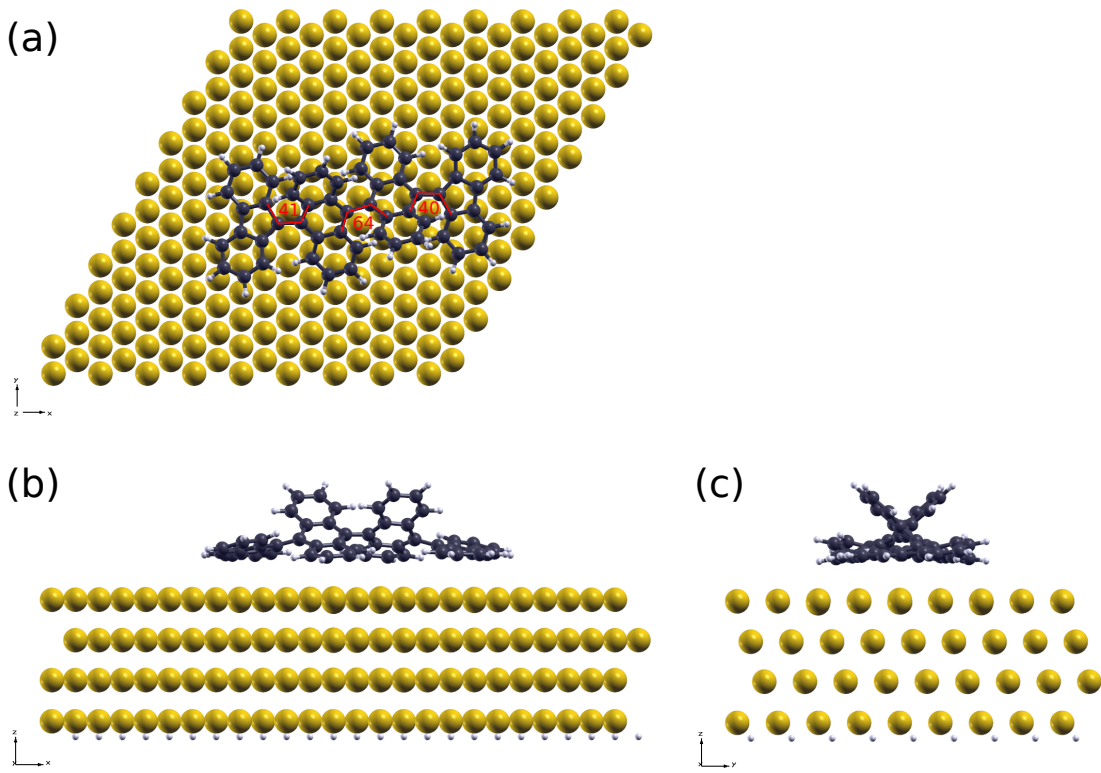


FIG. S13: Adsorption geometry of **2-OS** on Au(111) obtained with SIESTA. The three torsional angles indicated in panel (a) corresponds to $\theta_{\text{outer}}^{\text{surf}} = 40^\circ$ and $\theta_{\text{inner}}^{\text{surf}} = 64^\circ$. As reference, the corresponding angles in the gas phase were found to be $\theta_{\text{outer}}^{\text{free}} = 54^\circ$ and $\theta_{\text{inner}}^{\text{free}} = 71^\circ$.

3.3. Thermochemistry effects on DFT calculations

In the following section we will address the effects of considering thermochemistry (vibrations, rotational motion, etc.) to DFT calculations on **2-OS**. As it is discussed in the main text, according to MF-Hubbard calculations the open-shell $S = 0$ solution is lower in energy than the triplet. A variation of the angles $\theta_{o,i}$ affects the ΔE_{TS} energy separation, but it does not change the spin quantum number of the ground state. The effect of $\theta_{o,i}$ on the hoppings is calculated with a Slater-Koster parametrization in the case of MF-Hubbard, obtaining that ΔE_{TS} decreases when the angles are increased. The antiferromagnetic character of the kinetic exchange driven by hopping makes the $S = 0$ solution more stable, becoming degenerate with a $S = 1$ solution when two anthracene units, or an anthracene and an external fluorenyl unit, are perpendicular.

In Gaussian (g16)[14] it is possible to include the effects of temperature by the "freq" flag [15]. This flag entails the computation of different contributions to the entropy (S_{tot}) and internal thermal energy (E_{tot}). Specifically, this program considers the contributions from translation, electronic motion, rotational motion and vibrational motion. Then, it considers a thermal correction to the enthalpy and free energy, respectively, as:

$$H_{corr} = E_{tot} + k_B T, \tag{20}$$

and

$$G_{corr} = H_{corr} - T S_{tot}, \tag{21}$$

where $S_{tot} = S_t + S_r + S_v + S_e$ and $E_{tot} = E_t + E_r + E_v + E_e$ consider the different contributions that have been mentioned, where t , r , v and e refer, respectively, to the contributions from translation, rotational motion, vibrational motion and electronic motion.

By comparing the sum of electronic and thermal free energies for the $S = 1$ and open-shell $S = 0$ solutions ($G_{S,T}$) for different values of the temperature with a relaxed gas phase geometry ($\theta_i \approx 90^\circ$), we can conclude that the thermochemistry effects are responsible of the $S = 1$ ground state in gas phase (see Figure S14), since for low T the $S = 0$ is the ground state but very soon the $S = 1$ becomes more stable when the temperature is increased. Then, if the geometry is planarized, the $S = 0$ solution is stabilized in account of an enhancement of the kinetic antiferromagnetic exchange, in accordance with MF-Hubbard.

	PBE/STO-3G (5K)	PBE/STO-3G (100K)	BLYP/6-31G (5K)	BLYP/6-31G (100K)
ΔG_{TS} (meV)	0.7	-7	-0.2	-9

TABLE I: Difference in energy between the open-shell $S = 0$ and $S = 1$ solutions for different density functional/basis and temperatures. The geometries were relaxed for every S in gas phase and without thermochemistry.

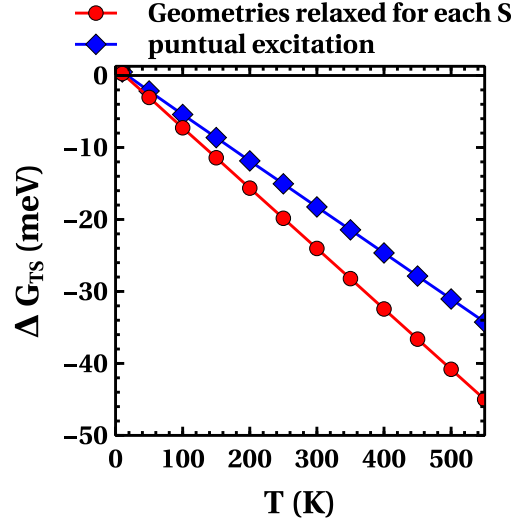


FIG. S14: Variation of $G_T - G_S = \Delta G_{TS}$ with the temperature (T), calculated with DFT. It was used the PBE exchange-correlation density functional [16] and the STO-3G basis [17, 18] with the Gaussian package[14] and the thermochemistry flag. For the red circles the geometry was relaxed for both spin solutions, and for the blue squares it was used the $S = 1$ relaxed geometry for all the calculations. The geometries were relaxed without the "freq" flag.

4. BIBLIOGRAPHY

- [1] Z. Zeng, Y. M. Sung, N. Bao, D. Tan, R. Lee, J. L. Zafra, B. S. Lee, M. Ishida, J. Ding, J. T. López Navarrete, Y. Li, W. Zeng, D. Kim, K.-W. Huang, R. D. Webster, J. Casado, and J. Wu, *J. Am. Chem. Soc.* **134**, 14513 (2012).
- [2] K. Tanaka, S. Kishigami, and F. Toda, *J. Org. Chem.* **55**, 2981 (1990).
- [3] H. Lee, M. Jo, G. Yang, H. Jung, S. Kang, and J. Park, *Dyes Pigm.* **146**, 27 (2017).
- [4] J. C. Slater and G. F. Koster, *Phys. Rev.* **94**, 1498 (1954).
- [5] H. Rezaei and A. Phirouznia, *Eur. Phys. J. B* **91**, 295 (2018).
- [6] N. Papior, “`sisl: v0.14.4.dev46+g8754d4f5`,” (2023).
- [7] S. Sanz Wuhl, N. Papior, M. Brandbyge, and T. Frederiksen, “`hubbard: v0.4.1`,” (2023).
- [8] J. M. Soler, E. Artacho, J. D. Gale, A. García, J. Junquera, P. Ordejón, and D. Sánchez-Portal, *J. Phys.: Condens. Matter* **14**, 2745 (2002).
- [9] M. Dion, H. Rydberg, E. Schroder, D. C. Langreth, and B. I. Lundqvist, *Phys. Rev. Lett.* **92**, 246401 (2004).
- [10] J. Klimes, D. R. Bowler, and A. Michaelides, *J. Phys.: Condens. Matter* **22**, 022201 (2010).
- [11] S. García-Gil, A. García, N. Lorente, and P. Ordejón, *Phys. Rev. B* **79**, 075441 (2009).
- [12] N. Gonzalez-Lakunza, I. Fernández-Torrente, K. J. Franke, N. Lorente, A. Arnau, and J. I. Pascual, *Phys. Rev. Lett.* **100**, 156805 (2008).
- [13] I. Horcas, R. Fernández, J. M. Gómez-Rodríguez, J. Colchero, J. Gómez-Herrero, and A. M. Baro, *Rev. Sci. Instrum.* **78**, 013705 (2007).
- [14] M. J. Frisch, G. W. Trucks, H. B. Schlegel, G. E. Scuseria, M. A. Robb, J. R. Cheeseman, G. Scalmani, V. Barone, G. A. Petersson, H. Nakatsuji, X. Li, M. Caricato, A. V. Marenich, J. Bloino, B. G. Janesko, R. Gomperts, B. Mennucci, H. P. Hratchian, J. V. Ortiz, A. F. Izmaylov, J. L. Sonnenberg, D. Williams-Young, F. Ding, F. Lipparini, F. Egidi, J. Goings, B. Peng, A. Petrone, T. Henderson, D. Ranasinghe, V. G. Zakrzewski, J. Gao, N. Rega, G. Zheng, W. Liang, M. Hada, M. Ehara, K. Toyota, R. Fukuda, J. Hasegawa, M. Ishida, T. Nakajima, Y. Honda, O. Kitao, H. Nakai, T. Vreven, K. Throssell, J. A. Montgomery, Jr., J. E. Peralta, F. Ogliaro, M. J. Bearpark, J. J. Heyd, E. N. Brothers, K. N. Kudin, V. N.

- Staroverov, T. A. Keith, R. Kobayashi, J. Normand, K. Raghavachari, A. P. Rendell, J. C. Burant, S. S. Iyengar, J. Tomasi, M. Cossi, J. M. Millam, M. Klene, C. Adamo, R. Cammi, J. W. Ochterski, R. L. Martin, K. Morokuma, O. Farkas, J. B. Foresman, and D. J. Fox, “Gaussian~16 Revision C.01,” (2016), gaussian Inc. Wallingford CT.
- [15] J. W. Ochterski, Gaussian Inc **1**, 1 (2000).
- [16] J. P. Perdew, K. Burke, and M. Ernzerhof, *Phys. Rev. Lett.* **77**, 3865 (1996).
- [17] W. J. Hehre, R. F. Stewart, and J. A. Pople, *J. Chem. Phys.* **51**, 2657 (1969).
- [18] J. B. Collins, P. von R. Schleyer, J. S. Binkley, and J. A. Pople, *J. Chem. Phys.* **64**, 5142 (1976).